

Diamonds as Potential Particle Detectors

Samuel Meier Jahn, Department of Physics

April 8, 2016

Primary Advisor:

Stephen Wagner, Department of Physics

Committee Members:

Stephen Wagner, Department of Physics

John Cumalat, Department of Physics

Robert Parson, Department of Chemistry and Biochemistry

University of Colorado, Boulder

Abstract

The efficiency behavior of two polycrystalline chemical vapor deposition diamond sensors was examined and compared on different types of CMS readout chips (ROCs), to investigate the degree to which the maximum efficiency is limited by the operational threshold of the ROC. It was confirmed that by having the diamonds on lower threshold ROCs their efficiencies could be dramatically improved. The diamond sensors reached maximum efficiencies of over ninety percent: LC750 reached an efficiency of 0.949 and LC500 reached an efficiency of 0.926. While neither diamond displayed one hundred percent efficiency, the evidence suggests that continuing to lower the operational threshold of the CMS ROCs will further increase the efficiency.

Introduction

In high energy physics, vertex detectors are particle sensors designed to reconstruct particles' trajectories, and as the name suggests, locate event vertices, from beam interactions, decays or scattering. The current mainstay vertex particle detectors are composed of silicon, which is well characterized and understood; however, as accelerators go to higher luminosities (as shall be the case for the HL-LHC, the High Luminosity Large Hadron Collider, an upcoming augmentation to the LHC), the amount of radiation that a detector must withstand and still stay highly efficient is increasing. A goal is that a detector should be able to endure $2 \times 10^{16} n_{eq} cm^{-2}$ over ten years. Carbon in the diamond phase shows the potential to become a more radiation hard substitute¹ for silicon [1].

The radiation hardness of diamond comes in part from the small mass of the carbon atom, as compared with a silicon atom. When an incoming particle scatters off a nucleus, the nucleus can fragment, creating nuclear shrapnel that can go on to create further damage in the sensor crystal. As a consequence of the lighter mass of the carbon nucleus, the debris from an impact with another lattice atom has a lower cross-section and is thus less damaging to the crystal lattice than would be an equivalent impact with a silicon nucleus. This is because the cross-section for an impact of a lattice atom with scattered

¹Thin silicon detectors, and 3D silicon sensors are other possible candidates for radiation hard detectors that are being investigated.

fragments goes up with mass, and silicon with its higher atomic number is able to produce more massive fragments, as well as being more massive itself.

Irradiated diamonds are not yet able to be efficient enough sensors to be practical as vertex detectors². Some believe that the primary reason behind this is that the current generation of readout chips (ROCs) are not able to operate at a low enough threshold for the full capabilities of diamond based detectors to be seen. The argument is that since diamond has a greater band gap than silicon, a ROC that has been designed to work well with silicon, when used with a diamond will likely be blind to small signals and a significant fraction of events will be missed. This is because it takes more energy to push an electron into the conduction band of the diamond crystal, and as a result the signal peaks at a lower charge, since a given amount energy will promote fewer electrons into the conduction band in diamond than silicon. This problem becomes more significant as radiation damage accumulates diminishing the diamond's maximum charge collection distance, or CCD (the mean distance an electron can travel through a medium) [3]. The CCD is also lower in polycrystalline diamonds than single crystal diamonds by a factor of two to three. This is due to the domain boundaries between different crystal lattices which can trap charges before they can leave the crystal.

Arbitrarily small signals cannot be detected. While there are myriad factors limiting the smallest visible signal, it is noise that constitutes the greatest barrier in this case. Electrical noise is generated as an inevitable byproduct of operating the ROC's electronics: noise could drown out and overwhelm the ROC's ability to process data. Thus a threshold is applied to exclude this electronic noise [4]. This may be done since the noise signals typically do not have much charge compared to the data signals, and the majority of the noise can be eliminated by simply imposing a lower charge cutoff on signals accepted for processing.

²Diamonds are currently being utilized as beam condition monitors (BCM) at both CMS and ATLAS. BCMs are used to watch for fluctuations in the particle beam, and trigger a shutoff procedure should the beam shift to a state that may damage the sensitive equipment used, such as the main detectors [2].

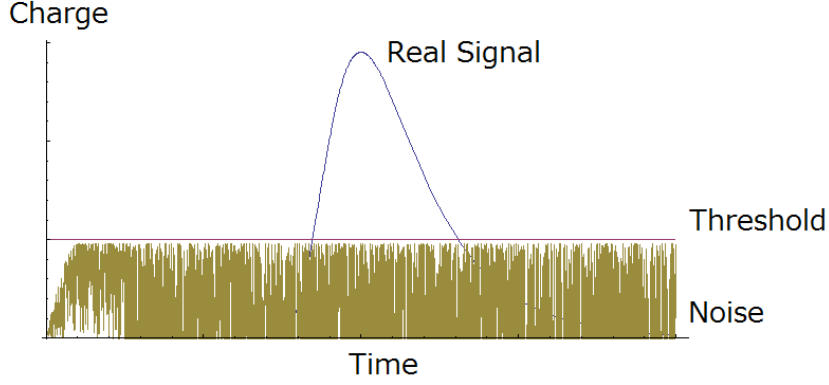


Figure 1: A signal (blue), noise (olive), and a threshold charge (magenta) are shown. The threshold is positioned low so as to allow as much signal passed as possible without letting the noise through.

As diamond detectors produce fewer high charge events than silicon, thresholds appropriate for silicon are too high for diamond, since too much real signal is also cut out. CMS ROCs that produce less noise could be run with a lower threshold, and hopefully this would allow more of the particle detection properties of diamonds to be seen. As CMS ROCs with lower operating thresholds are produced (currently the noise floor is around $2000e^- - 3000e^-$), the full extent of this issue may begin to become visible. In conjunction with testing new ROCs as they become available, the threshold dependence of diamond detector efficiency can be studied within the currently achievable range to try and draw some inferences on whether improving the threshold capabilities of the CMS ROC will be sufficient, or if there is another more serious obstacle that must (if possible or practical) be overcome if diamond is to serve as a detector material.

Diamond Production

The diamonds being investigated for detector use are made in a process called chemical vapor deposition (CVD), where gaseous hydrogen and a hydrocarbon (usually methane CH_4) are put under radical forming conditions using a plasma reactor. Within a limited range of conditions, diamonds can be made to grow.

Hydrogen is the majority species in the gas phase, while the hydrocarbon is much more rarefied, but both are critical. The hydrocarbon provides the carbon that will ultimately form the diamond. Much of the chemistry involved yet remains an enigma. Still it is believed that two carbon species, like acetylene, dictate crystal nucleation but are less significant during that actual growth; the methyl radical is thought to play that role. It is well known that under standard conditions sp^3 hybridized diamond is less thermodynamically stable than the sp^2 hybridized graphite. Here is where the hydrogen is believed to pull its weight, in the preferential etching of the undesired graphite [5].

If diamond crystals nucleate at multiple locations on the growing substrate, there is no guarantee that the lattice structures will line up correctly when the crystals eventually meet up during growth. This leads to polycrystalline CVD diamonds (pCVD). It is also possible for single-crystal CVD diamonds (scCVD) to be made through careful control of the growth and the use of diamond as a growing substrate, but these single-crystal diamonds are typically smaller than what is achievable by their polycrystalline counterparts [6]. The reason this is important is because single-crystal diamonds permit greater charge mobility, and thus allow for a higher charge collection distance, while polycrystalline diamonds are thought to have properties similar to a radiation damaged single-crystal diamond [3].

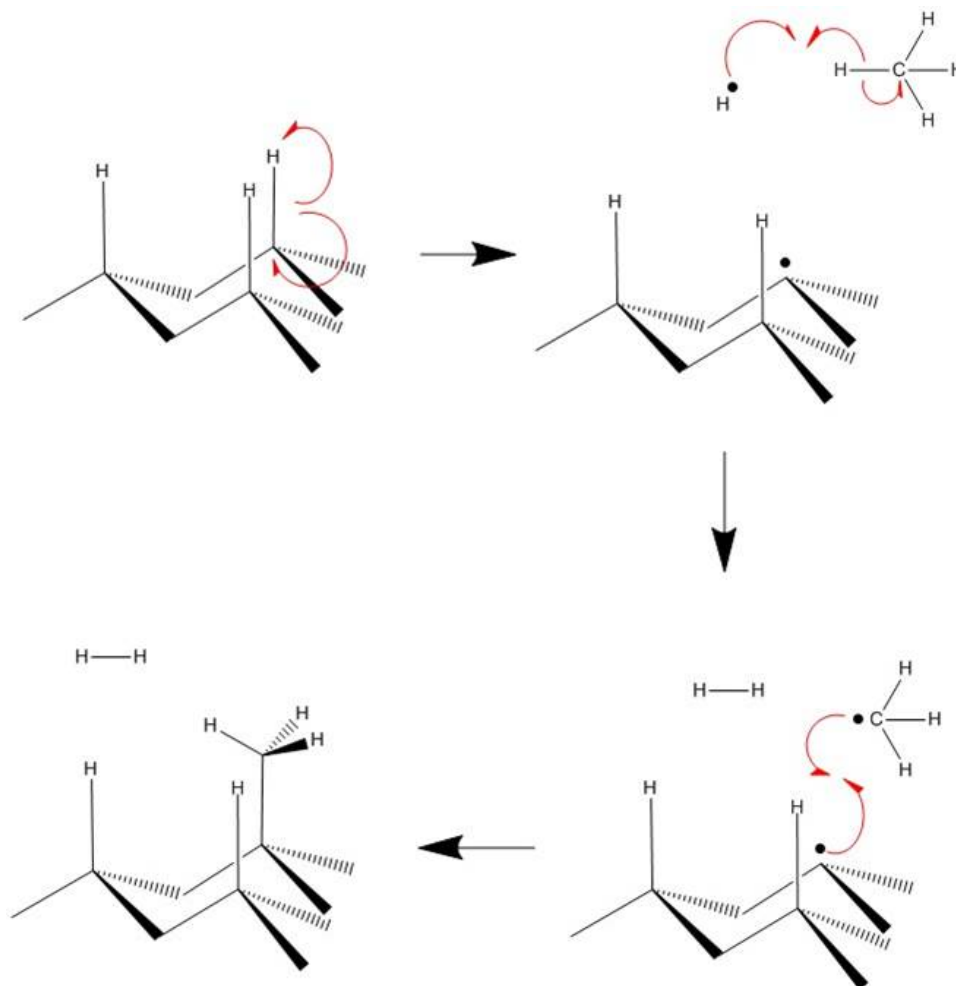


Figure 2: The above figure shows one of the multitude of possible mechanisms for CVD diamond growth. The vertices represent carbon atoms of the growing diamond (only a couple carbon atoms are shown out of the enormous number of carbons in a macroscopic diamond), while the dots represent unpaired electrons. The red curved arrows show the flow of electrons, while the black straight arrows indicate a step in the reaction sequence. Starting from the top left, a C-H bond is homolytically broken, initiating a pair of radicals. Following the arrow to the right, the atomic hydrogen propagates the radical by abstracting a hydrogen atom from a methane molecule, creating a methyl radical and molecular hydrogen. Following the reaction arrow down, the methyl radical is then able to form a bond on the growing diamond, terminating the radical process [7].

Signal Production and Detection

As a charged particle traverses the detector diamond, it interacts with the lattice electrons nearly continuously. This means that some electrons will get enough of an impulse to excite them into the conduction band of the diamond, where they are no longer bound to their parent carbon atom, creating a free electron and an electron hole [8].

The mean energy transferred to a medium per unit length, $\langle dE/dX \rangle$, depends upon the momentum of the particle (as well as medium and particle type). When a particle has a momentum such that $\langle dE/dx \rangle$ is at or near a minimum, the particle is referred to as minimum ionizing [10]. In diamond, a minimum ionizing particle or MIP typically produces about $36\ e^-/\mu m$ [9]. An applied electric field, typically around $1\ V/\mu m$ keeps the electron-hole pair from recombining, and pulls the electron-hole pair apart. The energy required to do this can be seen as a change in the current maintaining the electric field. The work required to separate the charges can be detected even when the electron-hole pair do not make it to the electrodes, just as long as the power drawn is large enough to be noticeable.

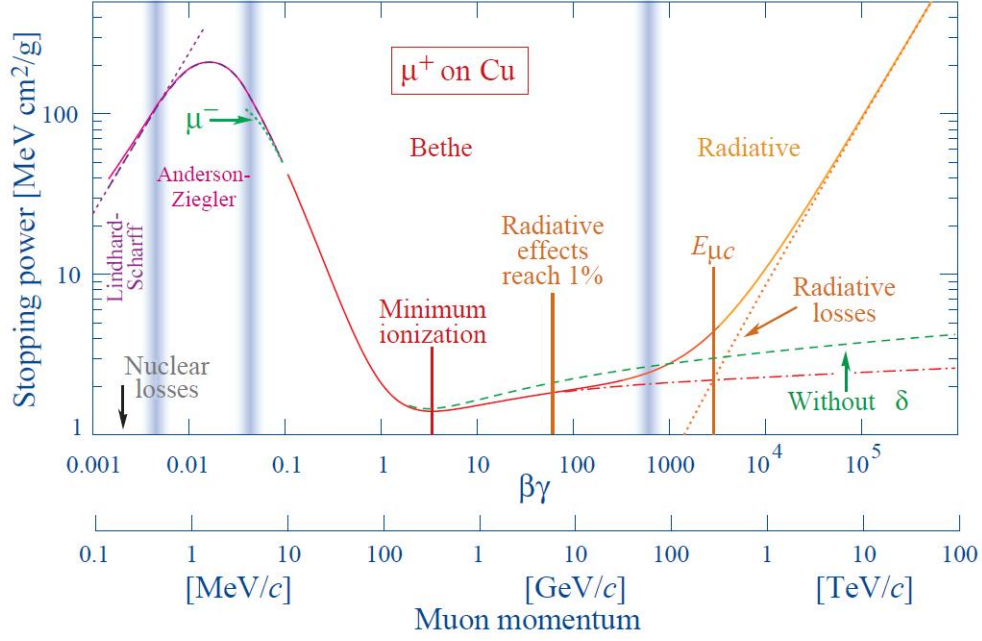


Figure 3: In the stopping power of copper from a muon $\frac{\langle dE/dx \rangle}{\rho_{Cu}}$ versus the muon's momentum [10], plot above the point of interest for this discussion is the function's minimum, labeled "Minimum ionizing". This minimum is more general than the muon through copper case, and a particle near the momentum of minimum energy loss (this may be different for different particles and different media) is known as a minimum ionizing particle (MIP).

Even once a mobile charge carrier is generated, the electrons and/or holes do not necessarily make it out of the diamond: traps, often located at the boundaries between crystals or at the sites of radiation damage can lock mobile charges in place within the diamond, preventing them from reaching an electrode. The number of these charge traps generally increases with non-ionizing energy loss (NIEL) by traversing particles. The predominant ionizing energy loss is thought to do significantly less damage [11].

The mean distance the electron-hole separate prior to being trapped is called the mean free path. The charge collection distance, or CCD is approximately equal to the smaller of the mean free path and the detector thickness. [12]. The CCD is easier to measure experimentally, since it can be shown that for MIPs

$$CCD = \frac{q_{collected}}{36e^-/\mu m} \quad (1)$$

(see [12] for more on the derivation).

Via a phenomenon known as pumping or priming, some traps may be saturated. The process involves exposing the diamond crystal to certain types of radiation, filling the charge traps so that they will be unavailable to catch signal electrons. The pumped or primed state can be fairly long enduring. The exception to this longevity coming from photons of the energy required to eject the charges from the traps, reactivating them [12].

An applied voltage has also been observed to depump the diamonds; during data acquisition at Fermilab in June 2015, turning the voltage off for even a half hour while the diamonds were in the 120 GeV proton beam of about 100,000 protons per minute was observed to increase their efficiency, everything else being left the same. The decrease in efficiency after being operated at voltage was also observed (see Fig. 29).

Spatial resolution can be dramatically improved using metal pixels on the grounded side of the diamond. Each pixel is connected to the ROC by an indium bump. For LC750 and LC500 (the diamond sensors being investigated here) the pixels are $100\mu m$ by $150\mu m$, as is standard among CMS pixel detectors. A high voltage pad is placed on the opposite side of the diamond.

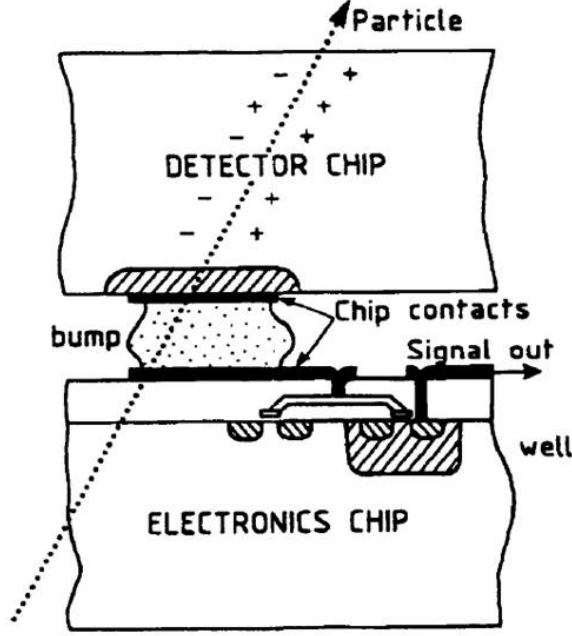


Figure 4: This illustration is of a bump and pixel [14]. The simplified depiction shows how the detector chip is not in uniform contact with the ROC across the electronics chip, but only at the site of a pixel. Any current flowing from the diamond to the ROC must pass through one of these pixels.

The Landau Distribution

The charge spectrum produced from a series of particles traversing the detector is to a good approximation proportional to the energy loss spectrum [15]. The spectrum of energy loss is approximately given by the well known Landau distribution.

In his paper *On the Energy Loss of Fast Particles by Ionization* Landau argues that a particle traversing a thin material of thickness x , has, for an amount of energy loss Δ , an energy loss probability density function, $f(x, \Delta)$, given by

$$f(x, \Delta) = \frac{1}{\xi} \phi(\lambda), \quad (2)$$

where ξ is a momentum dependent quantity that contains information on the medium the particle is traversing. Here the dimensionless λ is given in terms of the most probable energy loss, Δ_0 , as

$$\lambda = \frac{\Delta - \Delta_0}{\xi}. \quad (3)$$

Landau found that $\phi(\lambda)$ may be approximated by a function that now shares his

name.

$$Landau(\lambda) = \phi(\lambda) = \frac{1}{2\pi i} \int_{-i\infty+\sigma}^{+i\infty+\sigma} e^{-u \ln u + \lambda u} du, \quad (4)$$

where σ is a real positive number which determines the real part of the integration that remains parallel to the imaginary axis.

For the purpose of the data analysis here, the Landau function used is the one provided by the C++ based data analysis program, Root. The Landau approximation used is stated on the Root website to be “adapted from the CERNLIB routine G110 denlan” [16]. The denlan method of approximating the Landau distribution is reported to be accurate to seven significant figures, and to be better than the commonly used Moyal approximation [17].

Analyses

In the following analyses error bars on the plots have been suppressed. The large sample size pushes the statistical error small enough that the error bars are frequently smaller than the size of the markers on the plots. The largest sources of errors are systematic errors that would not be accounted for by the error bar calculations, so showing the error bars would over estimate the confidence level. Systematic and statistical errors are discussed where relevant.

In the following discussions, the threshold is given by the register setting VTh. The VTh measures how much the threshold level is suppressed, so a higher VTh corresponds to a lower threshold.

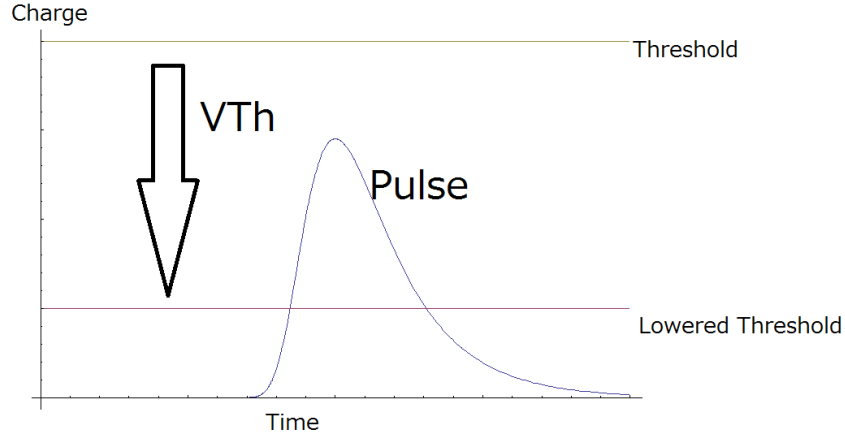


Figure 5: The VTh register setting pushes the threshold down; in the above diagram, the signal pulse can only be seen at the magenta lowered threshold, as the olive threshold is above the highest charge of the pulse.

The two diamonds under investigation are LC750 and LC500. Both LC750 and LC500 are polycrystalline diamonds with a thickness in microns indicated by the number in their names. LC750 has been radiation damaged at Los Alamos in December 2014. LC750 was irradiated by $(3.2 \pm 0.2) \times 10^{14} \frac{\text{protons}}{\text{cm}^2}$, with 800 MeV protons. To compare this with the standard 1 MeV neutron irradiation, a damage factor should multiply the proton dose. For silicon the damage factor for 800 MeV protons is 1.05. The damage factor for diamond is often taken as that for silicon; it may be slightly higher, but should still be on the same order of magnitude. Polycrystalline diamonds are thought to behave similar to a single crystal diamond after extended use and radiation damage[3]. By radiation damaging LC750 further, the ability of diamond to continue to function can be tested. This is important since for diamond to ever be a practical radiation hard detector medium, diamonds must be able to operate at near unit efficiency even after sustaining radiation damage. Sans this, diamond cannot be considered radiation hard, at least not in the desired sense.

⁹⁰Sr Data Collection and Analysis

The diamond LC750 was placed under a ⁹⁰Sr source, which decays into ⁹⁰Y via beta emission. The ⁹⁰Y also beta decays, but with electrons that are energetic enough to be seen by the detector. LC750 was left under the ⁹⁰Sr source for ten minutes while the data, processed by a CAPTAN (Compact And Programmable Data Acquisition Node) system [18], was recorded. This was done at four threshold register settings; $V_{Th} \in \{130, 135, 140, 144\}$, where higher register values correspond to lower physical charge thresholds. At too low a threshold, a register setting higher than $V_{Th} = 144$, there was too much noise to get a useful signal out of the sensor, so $V_{Th} = 144$ is the noise floor for this ROC.

During the data acquisition, a mask was placed on the noisy pixels. This is common practice and is used to separate electronic effects from detecting medium effects. Inefficiency due to misfiring pixels does not give information about the detecting efficiency of the diamond, and sometimes blocks the correct information from being read out.

For this study, we found that the CAPTAN did not function properly at the start of each session. The CAPTAN worked fine for the remainder of the session. The division in time between when the CAPTAN was working properly and when it was clean and consistent from run to run. This problem is from the CAPTAN system not LC750, and can be accounted for by cutting out the first part of data. This reduced the amount of data by the same amount in all four cases, so the following conclusions will not be affected. This sort of behavior is not uncommon for CAPTANs operated at the University of Colorado.

A charge calibration was performed to convert the circuit ADC output to the number of electrons collected. More details on charge calibrations will be presented later.

From the charge spectrum data, the number of events versus charge per event, for each run was fit to a function of the form

$$Charge\ Spectrum(q) = A * Erf[b(q - p0)] * Landau[(q - q0), width],$$

where A is an amplitude that is proportional to the total charge collected, q_0 a parameter to set where the Landau peaks, b a steepness parameter for the error function, p_0 the physical threshold (with units of charge), and q the charge and also the independent variable. The Landau distribution is the characteristic form of the data type (discussed earlier). The error function is a unit error function that goes between zero and one. The error function is used to model the threshold. The operational definition of the threshold is the charge at which the error function takes the value $\frac{1}{2}$.

Since each run was performed under the same radioactive ^{90}Sr source (which varies slowly enough in time that it produces a practically constant flux of radiation), and for the same length of time in the same position (a structure was used to ensure the correct positioning), the Landau distribution that multiplies the error function should be the same for all four tests; therefore, the fit was constrained by fixing the Landau and the amplitude to be the same for each run, leaving only p_0 to change between fits. The base Landau and the other parameters were still found from the fits, only they were fixed to be the same for all four data sets. The charge threshold that corresponded to the V_{Th} register value could then simply be read off the fit (p_0 in the plots in figure 6 on the following page).

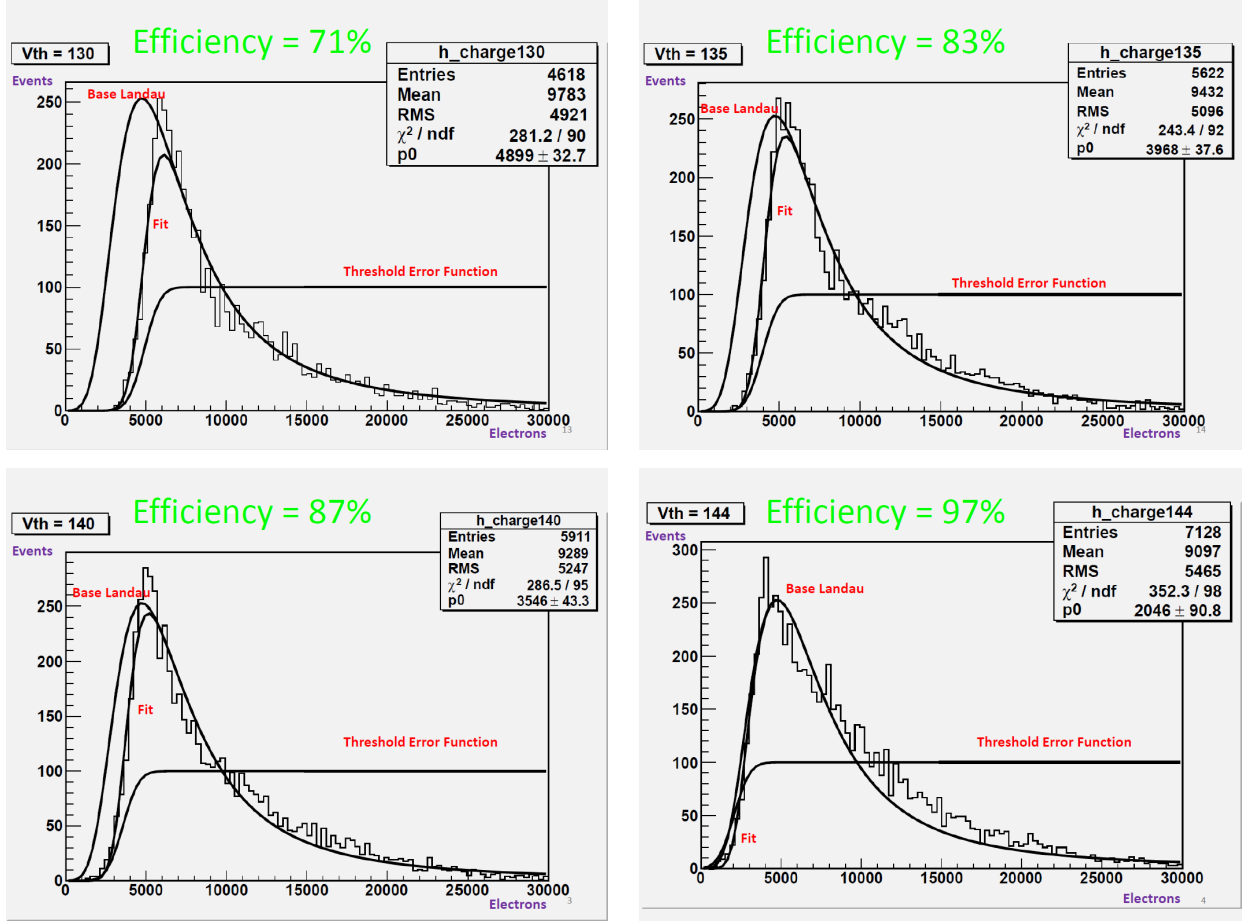


Figure 6: These plots show the charge spectra for four different threshold settings. The number in the upper left of each plot shows the VTh register value, the p0 in the upper right box shows the threshold in unit of e^- . There are three curves shown on each plot; the one that matches the spectrum the best is the actual fit. The fit is the product of the other two functions, the base Landau, which is the same for all four, and the threshold error function (scaled up for clarity), which differ only in where it turns on.

The lowest threshold is $2046e^-$, the p0 from the lower right plot in Fig. 6. So the noise floor of this ROC may be taken as approximately 2000 electrons.

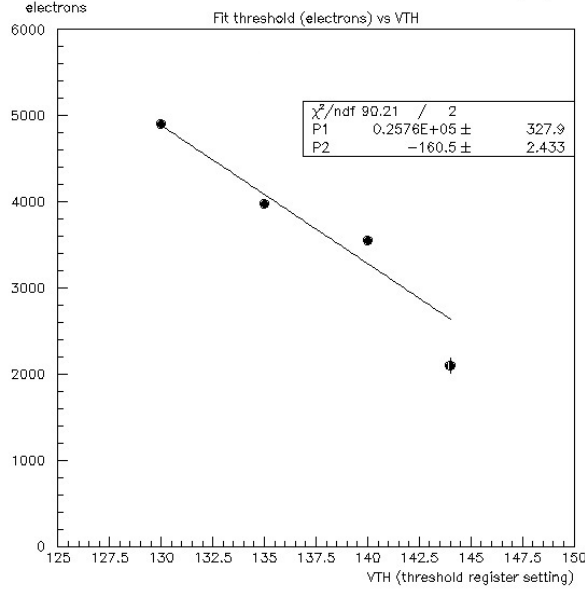


Figure 7: The threshold in electrons versus the VTh register setting that corresponds to the threshold was fit to a line. As can be seen the pattern, although monotonic, is not quite linear. There is not a strong expectation that it should be linear, but the fit still provides a tool for understanding the pattern.

Additionally, a rough estimate for the detector efficiency at each threshold may be made. This may be done by taking the ratio of the area under the fitted curve to that of the base Landau. This was done by integrating both curves from zero to 30,000 e^- , the upper range of the experimental signal. These are the efficiencies listed above each plot in Fig. 6. The efficiency versus VTh data are also shown in Fig. 8. The test beam studies discussed later will have more accurate values for the efficiencies.

These data may be combined to try and make some inferences on how the VTh threshold register setting affects the physical threshold in terms of electrons. Referring to Fig. 8, a general monotonic pattern may be seen, but more data would be required to find a functional form.

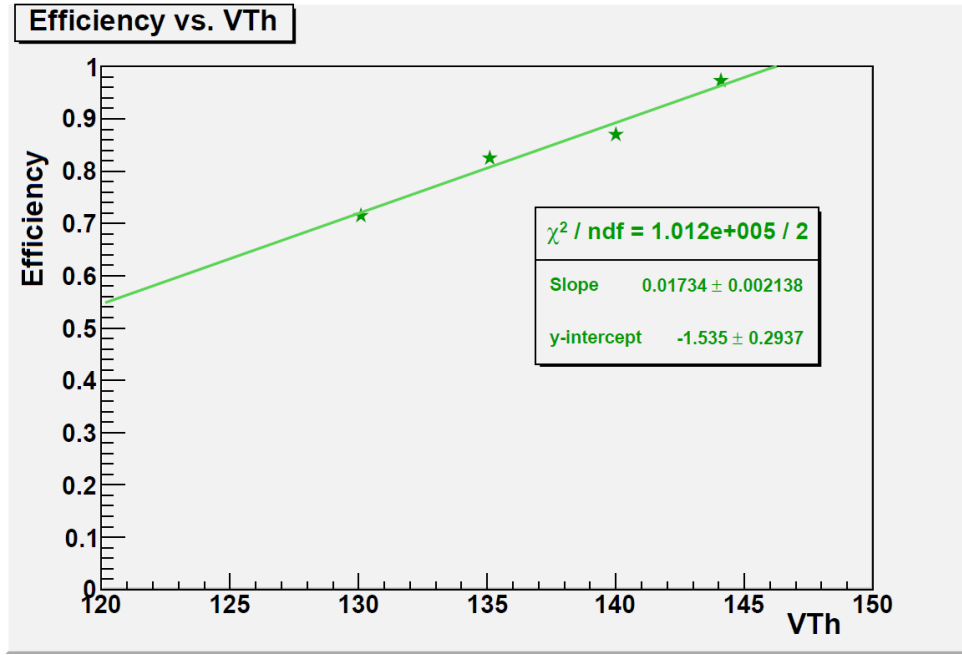


Figure 8: In this plot of efficiency versus threshold register value, the bench ^{90}Sr test efficiency is shown for the tested $\text{VTh} \in \{130, 135, 140, 144\}$. Following the fit passed the noise floor, the fitted curve equals one at $\text{VTh} = 146.2$.

Test Beam Data Analysis

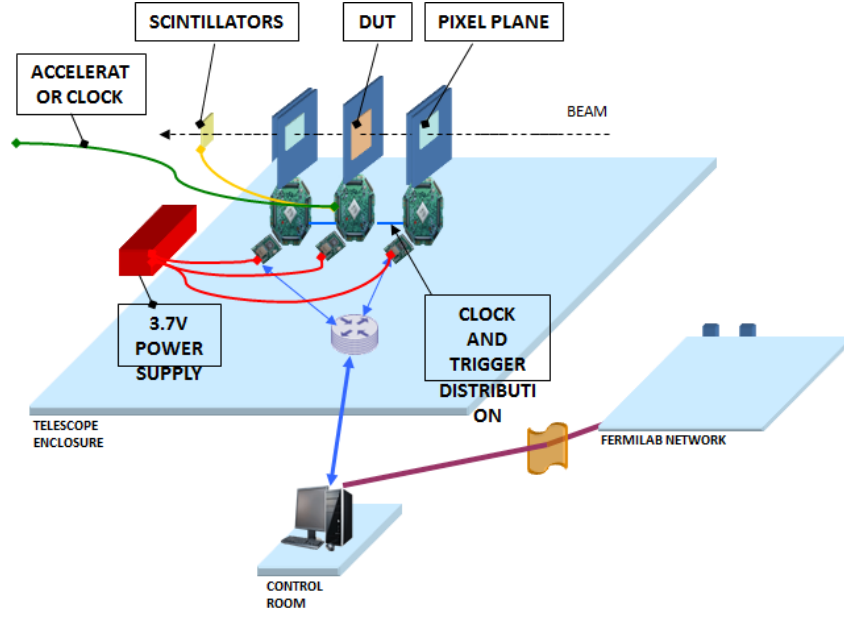


Figure 9: A schematic of the test beam setup, all the detectors are connected to CAPTAN systems. A detector under test (DUT), is shown between two other detectors; these form the telescope. There are more detectors in the telescope than shown here. During the June 2015 test beam there were four upstream telescope detectors and four downstream telescope detectors, and three DUTs.

A test beam, like the one at Fermilab, provides more control over experimental conditions than the ^{90}Sr . The time of charge deposition and the momentum of the beam particles are well known. The protons in the Fermilab test beam are approximately minimum ionizing (120 GeV). Also a series of well understood silicon detectors before and after the detector under test, DUT, provides a means to project where the protons hit the diamond sensors. By looking to see if a signal was produced from that pixel of the DUT, an efficiency, η , can be calculated.

$$\eta = \frac{n}{N}, \quad (5)$$

where N is the number of events projected by the telescope, and n is the number of events detected by the DUT.

2012 Test Beam Data Analysis

In the Spring of the year 2012, LC750 was sent to the Fermilab test beam, where it was subjected to numerous runs in the proton beam, under various conditions, and the sensor's output recorded. At this time it was bump bonded to a higher threshold, analog ROC.

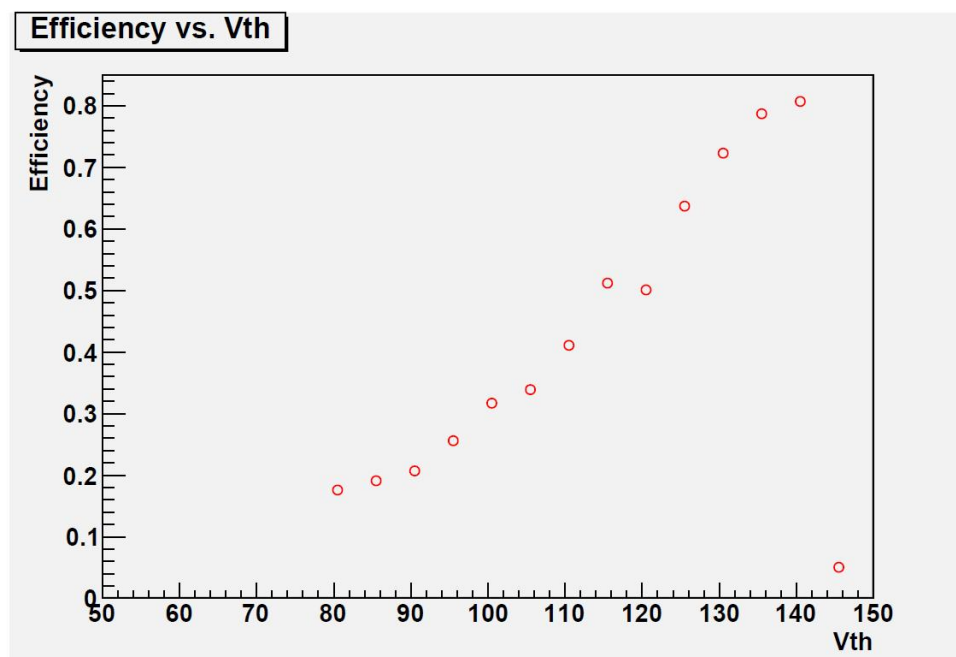


Figure 10: The efficiency versus threshold register value when no mask is applied, the low efficiency at $V_{Th} = 145$ is beyond the noise floor.

The data from a 16 run threshold scan was processed through Monicelli and Chewie, programs designed to reconstruct the particle tracks, and perform a preliminary analysis, respectively [19]. The overall efficiency was then plotted against the threshold register value. A clear relation can be seen in Fig. 10. The efficiency increases with threshold register value; in other words, the efficiency increases as the threshold decreases, up until the $V_{Th} = 145$, where the efficiency drops to about 0.05. As a $V_{Th} = 145$ is beyond the noise floor, this drop in efficiency makes sense. This V_{Th} is very similar to the one observed with the ^{90}Sr test at the University of Colorado (see previous section).

Since a significant amount of pixels were dead, a mask was imposed to limit future analysis to a good region of the detector. Since the dead pixels are due to the bumps not

being properly bonded, no information about the diamond is gained by including these pixels in the data analysis. With the mask on, the aforementioned efficiency analysis was repeated, and it was observed that the mean efficiency increased by a few percentage points.

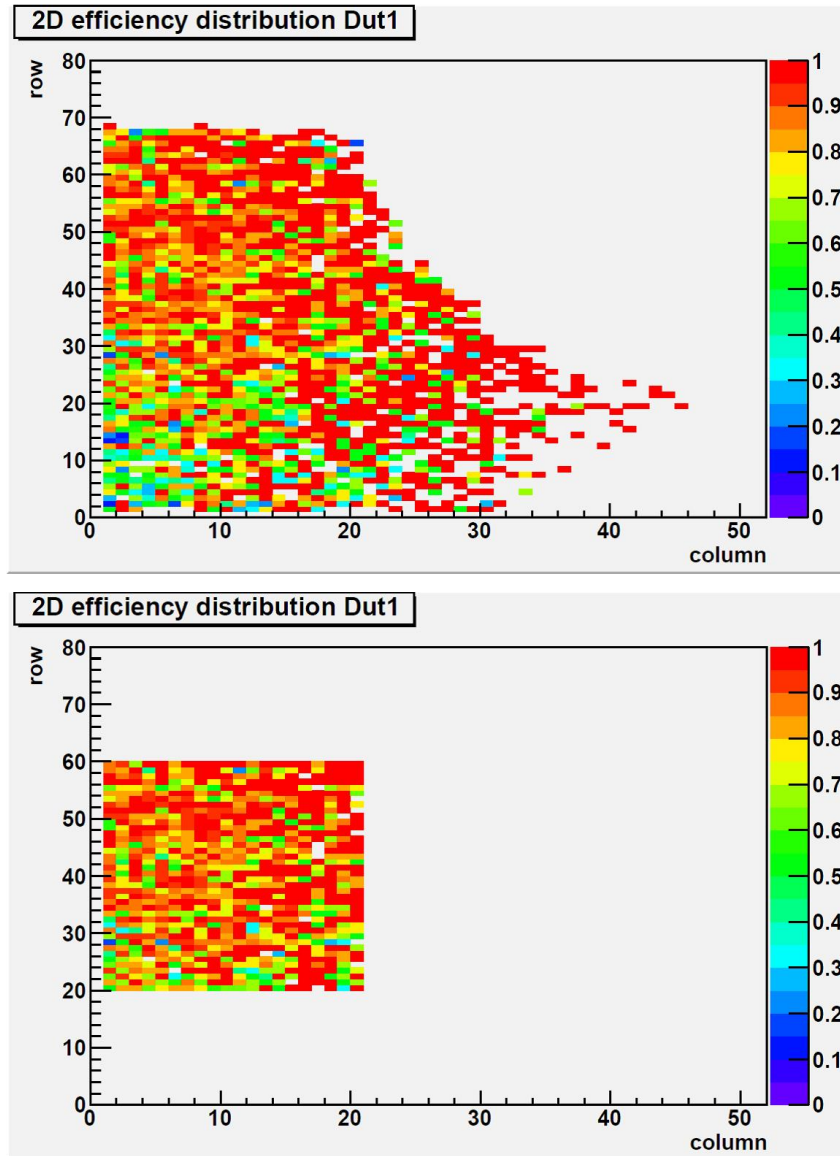


Figure 11: On the top is the un-masked data. As may be seen there are a lot of dead pixels. On the bottom is the same data, but with the mask on, leaving only rows $\in [20,59]$ and columns $\in [1,20]$.

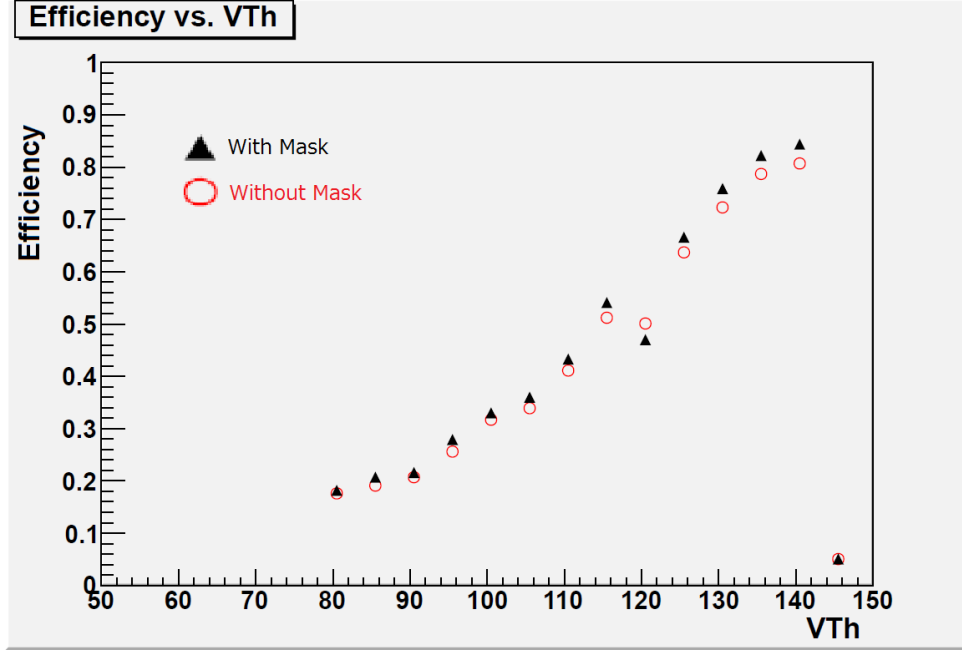


Figure 12: The efficiency versus threshold register value when the mask is shown in black triangles, superposed with the unmasked counterpart marked with red circles. Note the low efficiency at $V_{Th} = 145$, passed the noise floor. It is also interesting to note that among the data above the noise floor, every datum from the masked analysis has a greater efficiency, save the point at $V_{Th} = 120$. This is discussed in the main text.

Although there is no reason to suspect that the data points up to the noise floor should follow a linear pattern, they would be expected to be monotonic. This is because the threshold is cutting into the true distribution, which is purely non-negative, so lowering the threshold should only increase the efficiency. Once the noise floor is surpassed, other factors come into play and this argument is no longer valid. The efficiency at a $V_{Th} = 120$ is well below what would be expected: it is lower than the previous efficiency at $V_{Th} = 115$. This could indicate a systematic error, or it could simply be that there were not enough tracks traversing the detector during that run to get a good sample of the efficiency.

The $V_{Th} = 120$ run was a small run, containing only 249 tracks within the fiducial area. As the fiducial area consisted of 39 rows by 19 columns, there were 741 pixels for the 249 tracks. It is possible for one track to hit multiple pixels via a process called charge sharing, where in the charge signal produced by the traversing particle is distributed among two or more pixels, yet this is rare enough that full saturation of the 741 pixels

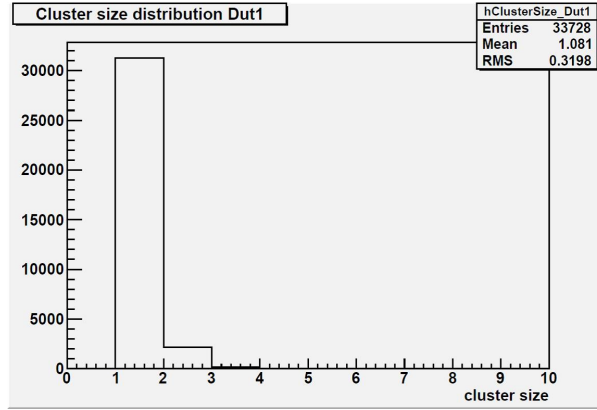


Figure 13: The above histogram shows the relative number of single pixel hits to double hits and so on. The actual numerical values on the y-axis are not meaningful since it is measured in arbitrary units, but the ratios of bin heights may be compared with the 249 tracks that produced this distribution. As can be seen nearly every track hit only a single pixel; about 229 out of the 249 tracks were single hits.

with 249 tracks is improbable to the level that it may be taken as impossible. While a low number of active pixels could indicate noise, in this case it was a run with low statistics; the number of tracks projected to traverse the detector was also small. And indeed, looking at the cluster size histogram, most of the pixels could not have been sampled. See Fig. 13.

Since so few events occurred, this is one case where statistical errors should be examined.

$$Error = \sqrt{\frac{\eta(1-\eta)}{N_{Tracks}}} = 0.03, \quad (6)$$

where $\eta = 0.50$ is the efficiency and N_{Tracks} is the 249 tracks. An efficiency of 0.50 ± 0.03 , is within three sigma of the midway point between the $VTh = 115$ point, and the $VTh = 125$ point.

These data may be superposed with the ^{90}Sr bench data discussed above. This provides a consistency check. The bench data may be more efficient than the test beam data since the ^{90}Sr beta particles deposit more energy than a MIP on average. The combination also narrows the region where the noise floor transition occurs.

The next series of test runs, which immediately followed the threshold scan, was a scan of the parameter Vana. The Vana is a voltage regulator for the ROC [20]. The

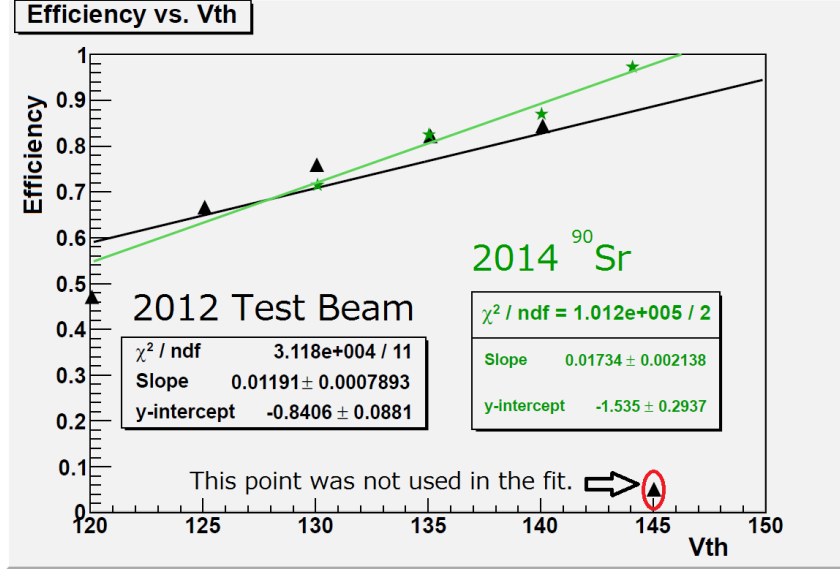


Figure 14: The efficiency versus threshold plot shows the ⁹⁰Sr bench data in green stars, and the masked 2012 test beam data in black triangles. Near the far right, the high efficiency green point is at VTh = 144, while the low efficiency black point is at VTh = 145. The straight line fit to the 2012 data does not include the low efficiency point passed the noise floor, since the data stops behaving linearly at the noise floor, but the fit does include all the other points. Not all of these are shown in this plot, but they may be seen in Fig. 12.

Vana parameter is not completely orthogonal to the VTh parameter, so both need to be examined. From these data a Vana dependence can be seen, but unlike with the VTh parameter, no sharp drop in efficiency was observed in the region surveyed.

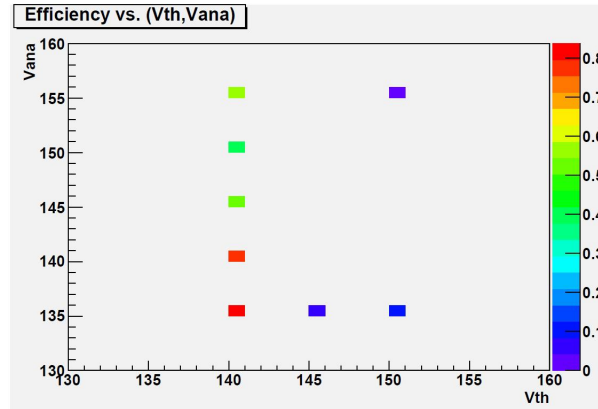


Figure 15: Above is a 2D histogram of the efficiency at different points in the VTh-Vana plane.

But looking along VTh = 140 in Fig. 15, it may be seen that the efficiency does indeed depend on Vana, as increasing Vana above 135 lowers the efficiency. The efficiency versus

VTh scan was conducted at Vana=135.

June 2015 Test Beam Data Collection Analysis

In June of the year 2015, the diamond sensors LC750 and LC500, which were then bonded onto new PSI digital ROCs were taken to Fermilab, where they were subjected to the accelerator's 120 GeV proton beam. The new ROCs should have a lower threshold than the older analog ROCs, so there was reason to believe that the maximum efficiencies should be higher than was found in the earlier two studies (the earlier LC500 test beam study was published in [3], and will be discussed). Around 150 separate runs were taken over the course of two days, June 15th and June 16th. The runs were on the order of two to five minutes, at 100,000 protons per spill, at one spill per minute. The proton beam was neither continuous nor exclusively used for the sensor testing, so the sensors during any run were exposed to the beam only periodically. Each bunch of proton that passed was called a spill. Preliminary results derived during the data taking suggested that both sensors could perform with efficiencies in excess of 0.9, higher than seen in previous experiments.

Charge Calibration

Before the test beam data could be analyzed in detail, a new charge calibration needed to be written. A charge calibration is a program that interprets the signal produced by the detectors to a physically meaningful metric, such as the number of electrons collected. The way this is done is to inject a known amount of charge into each pixel of each detector and read the output adc from the detector. This is done for many different amounts of charge. Once the data is collected, it is fit to a calibration fitting function. Then when deciding what charge a given adc corresponds to the inverse function is used. These programs usually use a hyperbolic tangent fit.

$$\textit{Standard Fitting Function} = p_0 + p_1 \tanh(p_2 \times \textit{adc} + p_3), \quad (7)$$

where p_n is the nth fitting parameter, and adc is the value reported from the detector. The reason a new calibration fit was needed was because of the behavior of the hyperbolic

tangent at low charge. As may be seen in the left image of Fig. 17, the hyperbolic tangent turns up away from the actual data. Normally this is not a problem, since typically the detectors are made of silicon, which with its lower band gap produces more charge per event. So signals from silicon have enough charge to avoid this region where the hyperbolic tangent fails. In the case of diamond, the higher band gap forces this region to become more important; some of the charge spectra were reporting a negative number of electrons on the low end of the charge spectra, not something that should be happening.

The new calibration fit was written to take advantage of the pre-existing framework of Monicelli and Chewie. The new fit was chosen to be a piecewise continuous function.

$$\text{Piecewise Fit Function} = \begin{cases} p_0 + p_1 \times q, & \text{for } q \leq q_{\text{transition}} \\ \text{adc}_0 + \sqrt{r^2 - (q - q_0)^2}, & \text{for } q_{\text{transition}} < q < q_0, \\ p_3, & \text{for } q_0 \leq q \end{cases} \quad (8)$$

Here r , $q_{\text{transition}}$, q_0 , and adc_0 are derived from the fit parameters. Using basic geometry it may be shown that for $a := \text{Tan}^{-1}(p_1)$,

$$q_0 = p_2, \quad (9)$$

$$r = \frac{p_0 + p_1 \times q_0 - p_3}{\text{Tan}(a)\text{Tan}(a/2)}, \quad (10)$$

$$\text{adc}_0 = p_3 - r, \quad (11)$$

$$q_{\text{transition}} = q_0 - r \times \text{Tan}(a/2)(\text{Sin}(a) + \text{Cos}(a)). \quad (12)$$

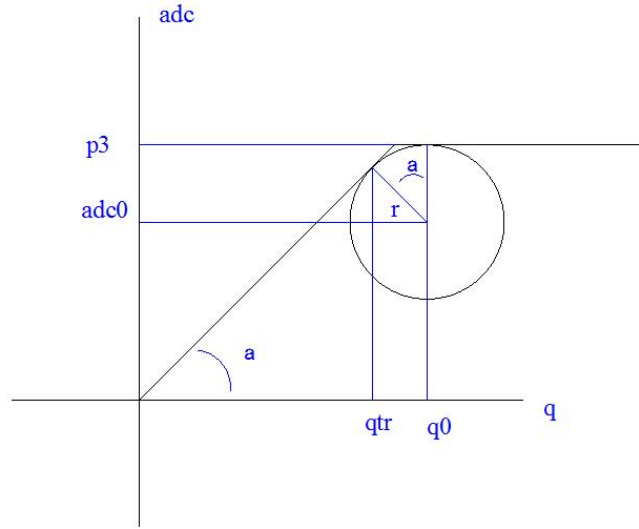


Figure 16: A diagram showing the relevant variables used in the calibration fit function is shown.

The new fit more closely matches the shape of the calibration curve, especially at low charges. Using this fit the diamonds' charge spectra no longer suffered from unrealistic negative numbers of electrons and also more closely resembled the expected Landau distribution. The two fits for a sample pixel are shown in Fig. 17, and representative charge spectra are shown in Fig. 18.

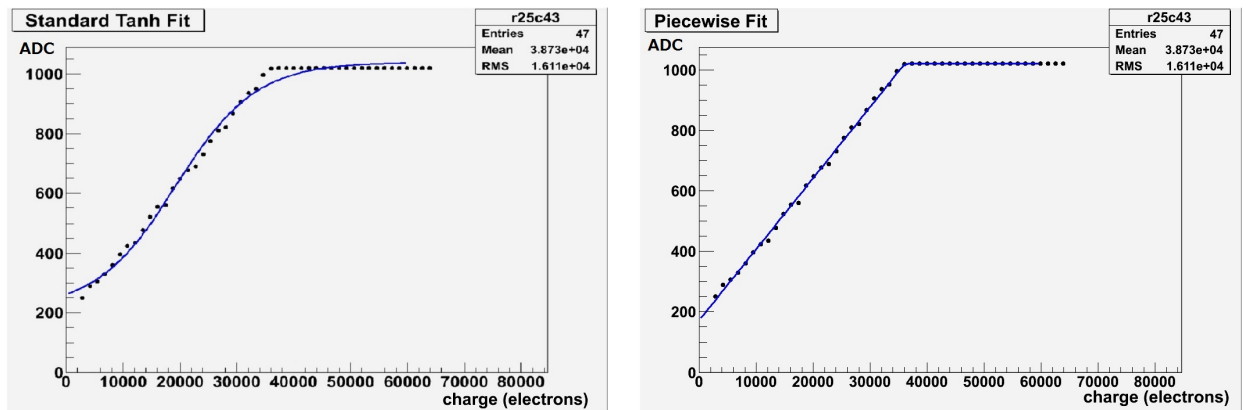


Figure 17: The same calibration data for a representative pixel, the pixel is on LC750 at the 25th row and the 43rd column. On the left is the standard fit, and on the right is the piecewise fit. As may be seen, the piecewise fit follows the pattern better. The piecewise fit is better able to accommodate the behavior at low charge. The piecewise fit also fits the data better as the adc becomes saturated.

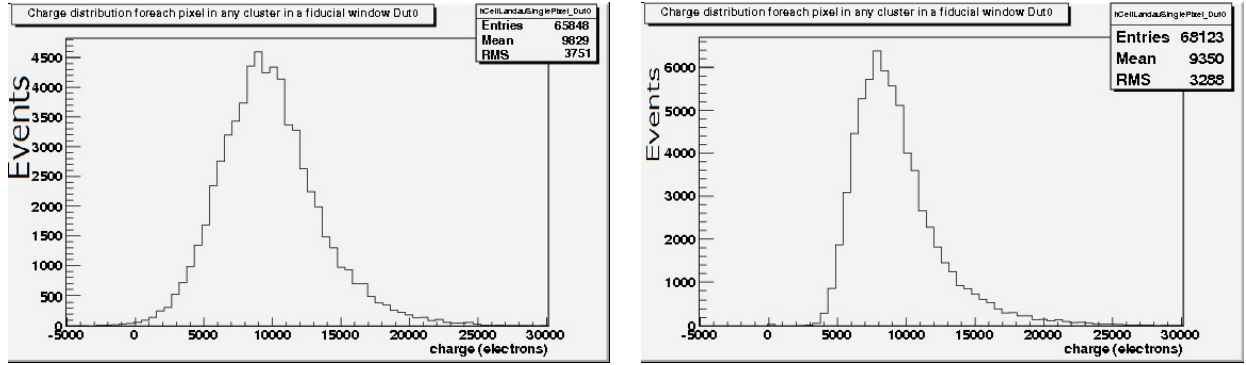


Figure 18: The charge spectrum that results from using the standard hyperbolic tangent charge calibration fit is on the left, and the charge spectrum that results from the piecewise fit is on the right. These charge spectra are both from the DUT LC750. Note that the standard calibration produces a charge spectrum that does not look like a Landau distribution and that the standard spectrum has charge less than zero electron events. The high charge side of both spectra look similar. This reflects the fact that both calibration fits agree well for higher charge values. Although the piecewise calibration fit was used on the telescope of silicon detectors, no practical difference was made by this substitution. The reason is that diamond has more of its charge spectrum at the lower end than silicon, one of the places where the piecewise fit is superior. The standard hyperbolic tangent fit thus works well for silicon based detectors like the telescope sensors, as well as most detectors. This likely explains why the standard fit is the hyperbolic tangent function rather than the more complicated piecewise function.

LC750 Analysis

Efficiency Analysis : High Voltage

One of the scans done was a high voltage (HV) scan. The high voltage is the applied voltage across the diamond to collect conduction band charge. The voltage was varied from 750 V or $1V/\mu m$ to 1000 V or $1.33V/\mu m$. As may be seen in the data plot, there is no practical advantage to increasing the applied voltage beyond 750 V, as long as the threshold is sufficiently low.

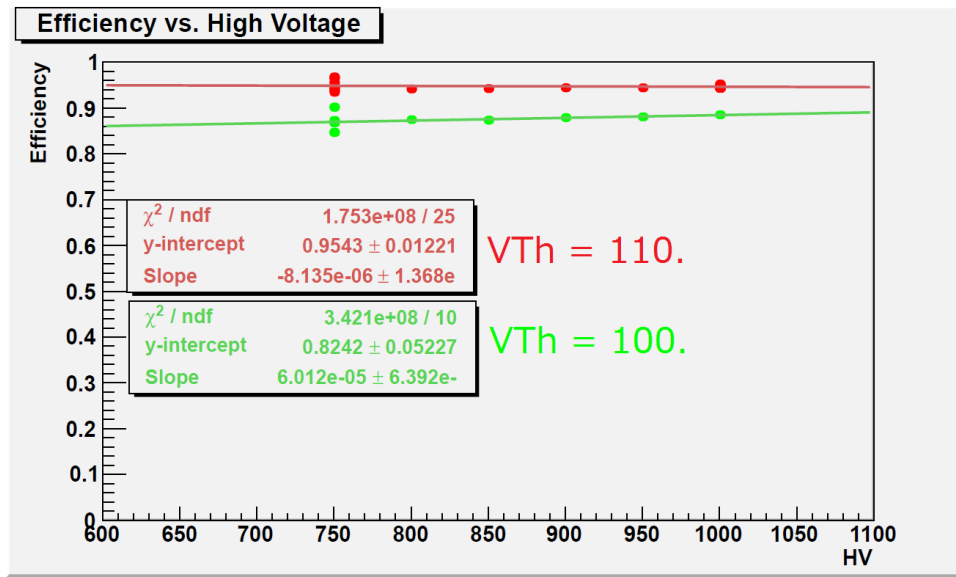


Figure 19: Above is a plot of the measured efficiency at various voltages. The red points are from a high voltage scan at $V_{Th} = 110$. And the green points are from a high voltage scan at $V_{Th} = 100$. The lower V_{Th} data (green), shows a slight positive slope, while the upper V_{Th} data (red) is practically flat.

Efficiency Analysis : V_{Th}

In the associated data plots (Fig. 20, and Fig. 30), the green data points are from the first half of the test beam data. These were taken on 2015-06-15 and 2015-06-16. The blue points come from the second half, 2015-06-16 and 2015-06-17. As may be seen, the runs from the second half are unanimously more efficient for a given V_{Th} than the runs from the first half of the data collection, even though the experimental conditions should be the same. All the documents regarding these runs were reviewed to look for any

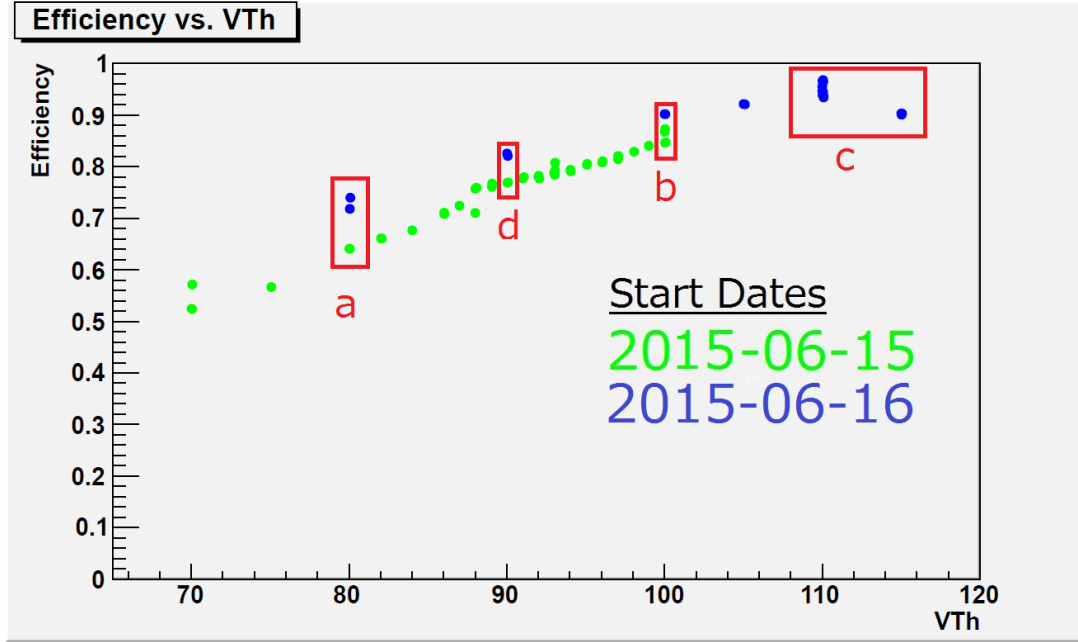


Figure 20: The efficiency versus VTh threshold value plot is for all the LC750 data taken during the June 2015 Fermilab visit with a high voltage of 750 V. The green points are from the first half of data collection, while the blue points are from the second half. The apparent shift in efficiency displayed by the blue points for a given VTh, which would be expected to match the green points better is discussed in the main text. Some important regions are marked. The main points discussed in the text are these points. For (a) at VTh = 80, the discrepancy between the blue and green points is greatest. At (b) the points at VTh = 100 there is an example of pumping between the green points. And (c) is where the efficiency begins to decline with increased VTh. The points at (d) are at VTh = 90, and provide counter evidence to the pumping hypothesis discussed later in the text.

differing register value or voltage difference that might explain this efficiency discrepancy; none were found.

It was briefly considered that a per pixel threshold adjustment might have been added in between data taking sessions. The 4160 pixels are not exactly the same, so when a particular threshold is set for the detector as a whole, each pixel responds slightly differently, and may have a threshold lower or higher than the average. This can be corrected for by measuring the threshold of each pixel and adjusting it with an offset so that when the detector gets set to a particular threshold, the pixels also get set to that threshold. Upon comparing when the adjustment program was written and when the efficiency data was taken, it is most likely the case that the adjustment was active for all the data, both green and blue data, so a per pixel threshold adjustment does not explain the efficiency mismatch the data displays.

If the beam were turned on early in the morning, and the detector was left in with no applied voltage, it could have become pumped. The records do not say whether or not this happened. Pumping is a well established phenomenon, and the size of its influence is typically smaller than that of the efficiency jump seen between the first half and second half of data collection. Nonetheless, the charge spectra of runs taken under analogous condition during the first half and second half were compared. Fortunately there is a set of runs all at $V_{Th} = 100$, (b) in Fig. 20, where not only are there runs from both data collection halves, but runs from the first half where the detectors were intentionally pumped, so the pumping phenomena may be directly compared to the differences seen before and after the efficiency jump. The green points at $V_{Th} = 100$, also provide a scale for the size of the pumping effect. As may be seen in Fig. 21, the mean charge in the pumped run is greater than in the pre-pumped run. This makes sense, for more charge traps are filled in the primed state, less charge gets lost, and each event produces more detectable charge.

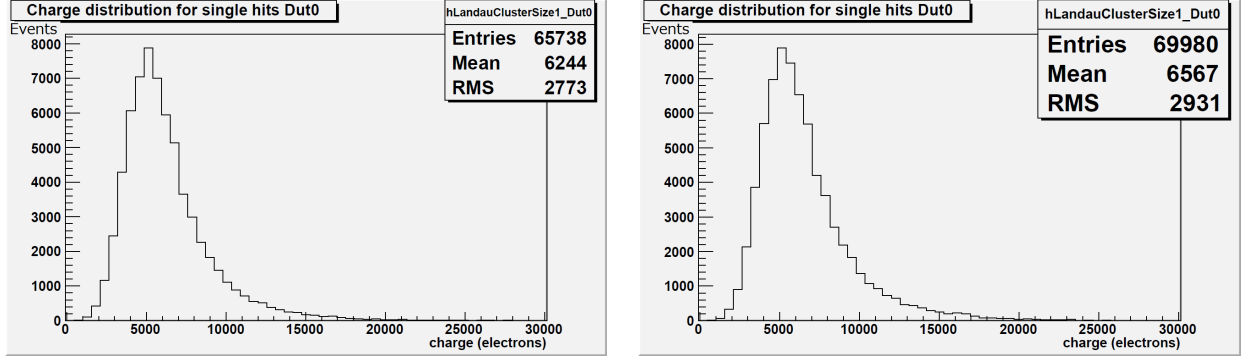


Figure 21: These charge spectra are from $V_{Th} = 100$. They are both green points and are at different efficiencies, shown in (b) in Fig. 20. The one on the left is from Run 912, has the lower efficiency and represents a pre-pumped charge spectrum. The one on the right is from Run 919, has the greater efficiency and illustrates a pumped spectrum. The only change made between these two runs was that the voltage across LC750 was turned off for several runs, and the diamond was allowed to sit in the beam for this time. The increase in charge output is small but clear.

Comparing these charge spectra to an analogous run from the blue data from the second half of data collection, the mean charge is higher still, but upon examining other runs there is no consistent pattern. Some runs like the green and blue points labeled by (b) in Fig. 20 show an increased mean charge with increased efficiency in agreement with the pumping hypothesis, as seen in Fig. 22, while other runs, like the runs labeled by (d) in Fig. 20 show the reverse, as seen in Fig. 23. It thus seems unlikely that pumping alone explains the efficiency jump.

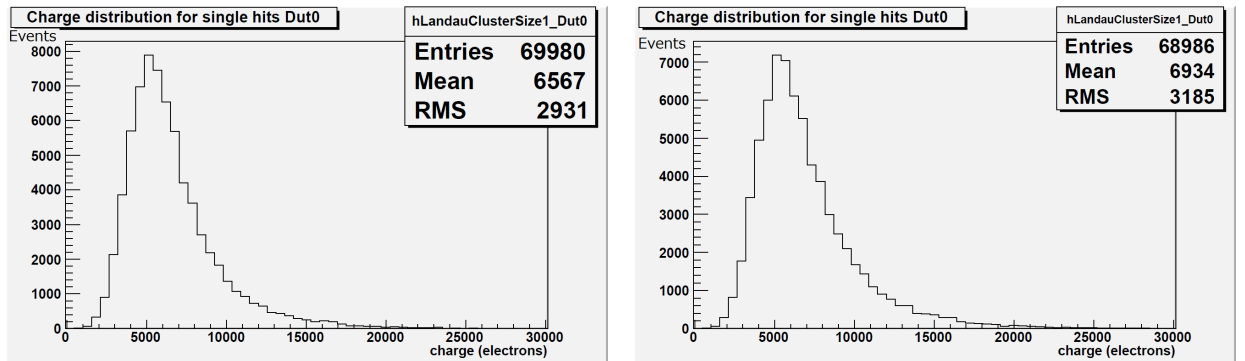


Figure 22: Both charge spectra are at $V_{Th} = 100$, and are labeled by (b) in Fig. 20. The charge spectrum on the left is again from Run 919, and is the highest efficiency green point labeled by (b) in Fig. 20. It has the less mean charge at $6567 e^-$, than Run 943 (the blue run of (b) in Fig. 20) with $6934 e^-$ of the right charge spectrum.

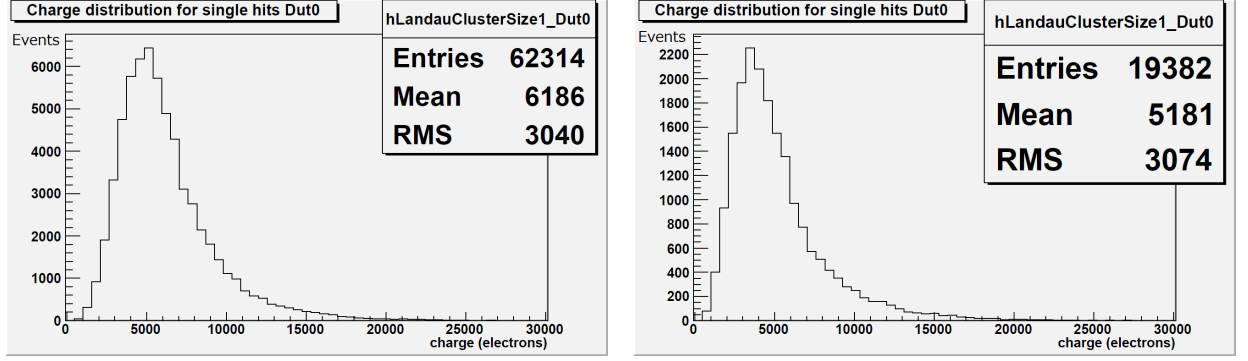


Figure 23: Both charge spectra are from the $V_{Th} = 90$ data, and are labeled by (d) in Fig. 20. The charge spectrum on the left is from Run 890 and is the green point, the point with the lower efficiency, yet it also has the greater mean charge at $6186 e^-$, as compared with the $5181 e^-$ of the right charge spectrum, which comes from the higher efficiency blue Run 940 of (d) in Fig. 20.

During an access period, when the detectors were being adjusted, the relative location of LC750 within the beam spot moved. If LC750 has areas of differing efficiency, which is possible among these detectors, then the jump in efficiency may be due to LC750 being re-positioned during the second half of the data collection so that a higher efficiency area got placed nearer the center of the beam, where it would receive a greater proton flux.

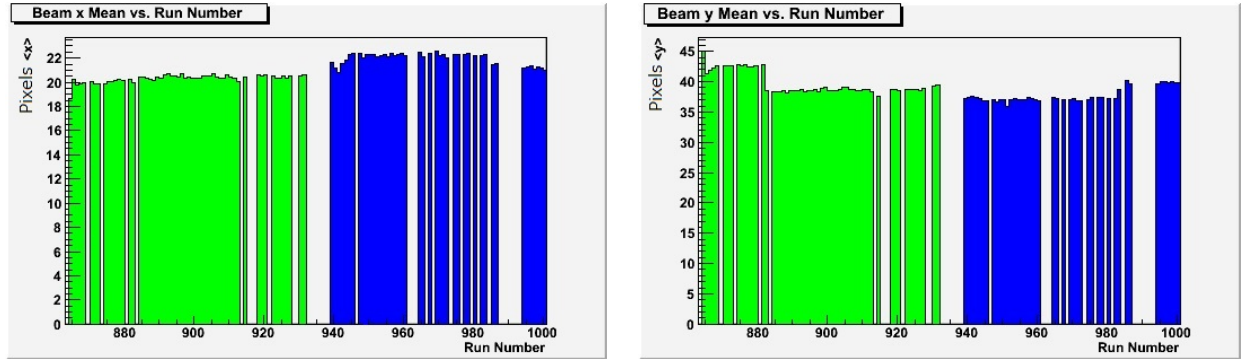


Figure 24: The above shows the mean pixel of the beam on the detector, not the beam itself, as the center of the beam is off the detector. Both the mean x pixel and mean y pixel change during the gap between the green and blue data (colored the same as in Fig. 20), both by about two pixels. Since a pixel is $150\mu m \times 100\mu m$, this corresponds to a shift in the mean position of $\sqrt{300^2 + 200^2}\mu m = 360\mu m$.

To test this hypothesis, the detector with LC750 was divided into four quadrants by applying one of four masks to the data, one for each quadrant. From each set of conditions that had a run from the first half of the data collection and one from the second half,

representative runs were selected. Each quadrant from these runs was then separately analyzed for efficiency. Figure 25 shows plots of efficiency versus quadrant number for a green run and a blue run in (a) in Fig. 20, both at $V_{Th} = 80$. These runs show the behavior that all the others analyzed by quadrant demonstrate; while some quadrants are more efficient than others, no quadrant differs enough from the others for the detector's change of location in the beam to explain the efficiency jump.

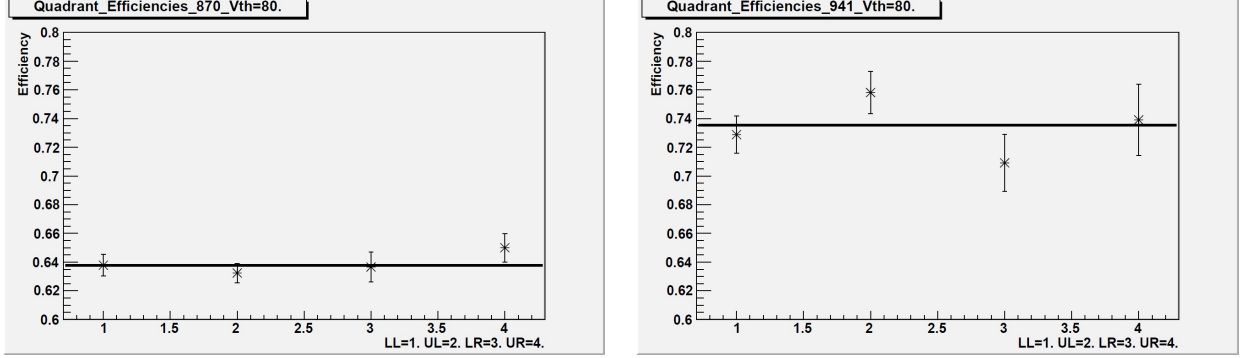


Figure 25: The efficiencies in different quadrants of the detector, the plot on the left is from the first half of the data collection. And the point on the right is from the second half of data collection. Both runs were taken under the same conditions at $V_{Th} = 80$. No quadrant is more than two sigma away from the detector efficiency. This is not enough for regional differences in the sensor efficiency to explain the efficiency discrepancy between the first and second halves of data collection. The lower left quadrant is 1. The upper left is 2. The lower right is 3, and the upper right is 4.

Another possibility is noise. If there is a hot pixel, a pixel that misfires and overloads the electronics, real data can get lost and the efficiency would go down. It is possible that a mask was placed on LC750 to remove the ill effects of one or more hot pixels. To test this hypothesis, the pixel efficiencies were added together for all the runs that occurred during the first half of data collection, and during the second half of data collection. The logic behind this was that if a mask were applied then the pixel would have no entries, and by adding many runs together the statistical probability that a pixel will be missed by chance is greatly reduced.

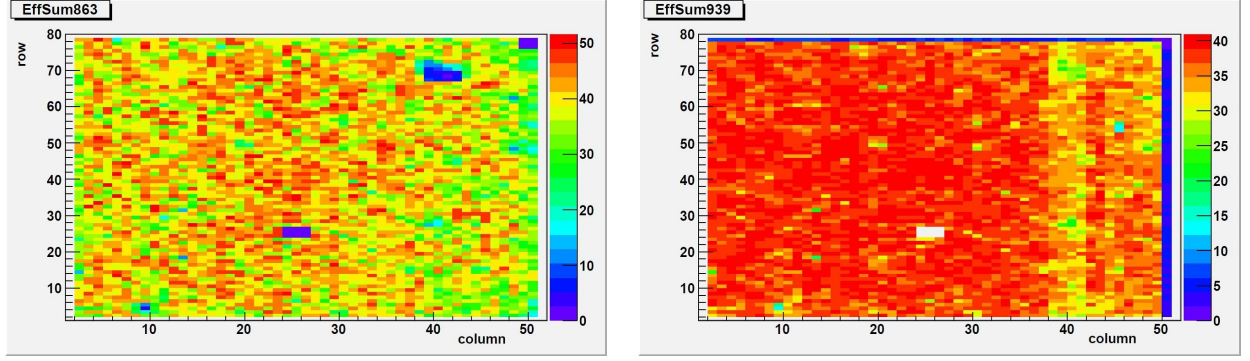


Figure 26: The above plots show the sum of the efficiencies for each pixel during the first half of data collection (left), and for the second half (right). Save for the nine pixels centered at row 25 and column 25, every pixel that has data during the first half also has data during the second half of data collection. All three low regions with little data in the left plot are regions where the pixels were only active for a few runs. These runs were examined and the efficiency of the regions was consistent with the rest of the detector. For an example see Fig 27.

As shown in Fig. 26, the only pixels that received data in the first half but not the second half of data collection were those of the three by three square centered at row 25 and column 25. Upon further examination only a single run, identified by the run number 892, during the first half actually had any data in these pixels. The pixel efficiency map for Run 892 is shown in Fig. 27. While it is a mystery why these pixels worked during only this run, there is nothing strange about either the data itself or about where it fits into the pattern set by the others runs, so this mystery is innocuous and not relevant to the efficiency jump enigma.

Referring back to Fig. 26, the right hand histogram, from the second half of data collection, shows a row and a column that received very few data, the right column and top row. Upon tracking the data in these pixels to their source runs, it was found that only the first several runs from the second half of data collection had any data for these runs. This suggests that noisy pixels were masked out. Indeed the run just prior to when the mask was applied displayed a low efficiency in the far right column, as would justify the mask (shown in Fig. 28). However the most puzzling runs, the two high efficiency runs at $V_{Th} = 80$, (a) in Fig. 20, were taken before the mask was applied. So a mask was applied as hypothesized, but not in a way that could explain the efficiency discrepancy.

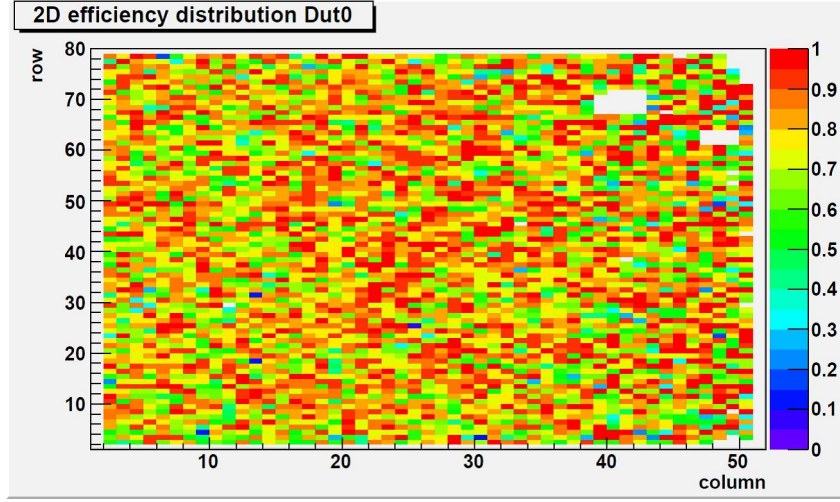


Figure 27: Here is the efficiency map for LC750's single run where the nine pixels centered at row 25 and column 25 had data. On its own, there is nothing abnormal about this run.

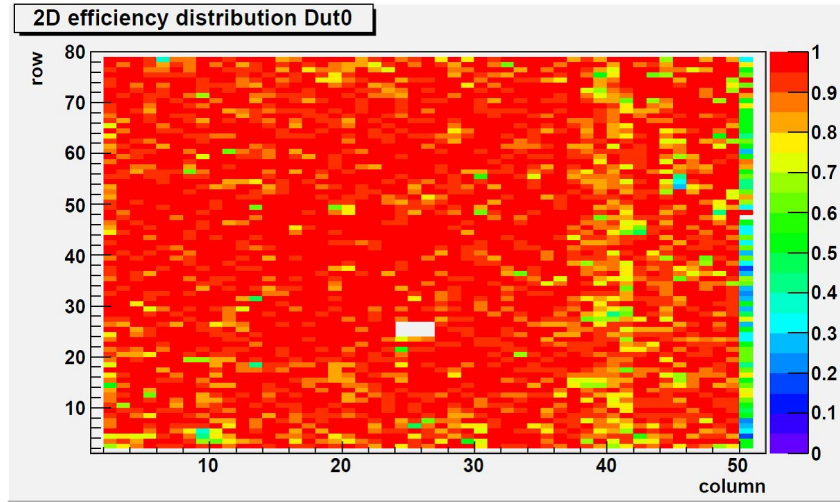


Figure 28: Above is the efficiency map for LC750's run just prior to when the mask was applied. As can be seen, the far right column has a relatively low efficiency.

It is still unclear why the two data sets do not line up as expected. Despite the earlier stated evidence against pumping, priming yet still may explain it. At higher thresholds the pumping effect could reasonably be larger. The higher threshold improvements should come from the events that barely made it passed the threshold charge, those that would not have made it if there were more charge traps, as there would be in the un-pumped state. However, it is not known whether or not the test beam was indeed allowed to pump LC750 the morning of 2015-06-16. This possible pumping combined with the lack

of clear evidence for pumping in the available data means that while pumping may be the most likely explanation, it is far from certain.

In regard to pumping an instance of depumping was observed. One of the final tests done on LC750 was to turn off the applied voltage, and pump it for 20 to 30 minutes. Then data was taken run after run holding every non-temporal parameter fixed as was possible. Figure 29 shows the data, where a fairly rapid depumping of several percent per hour can be observed.

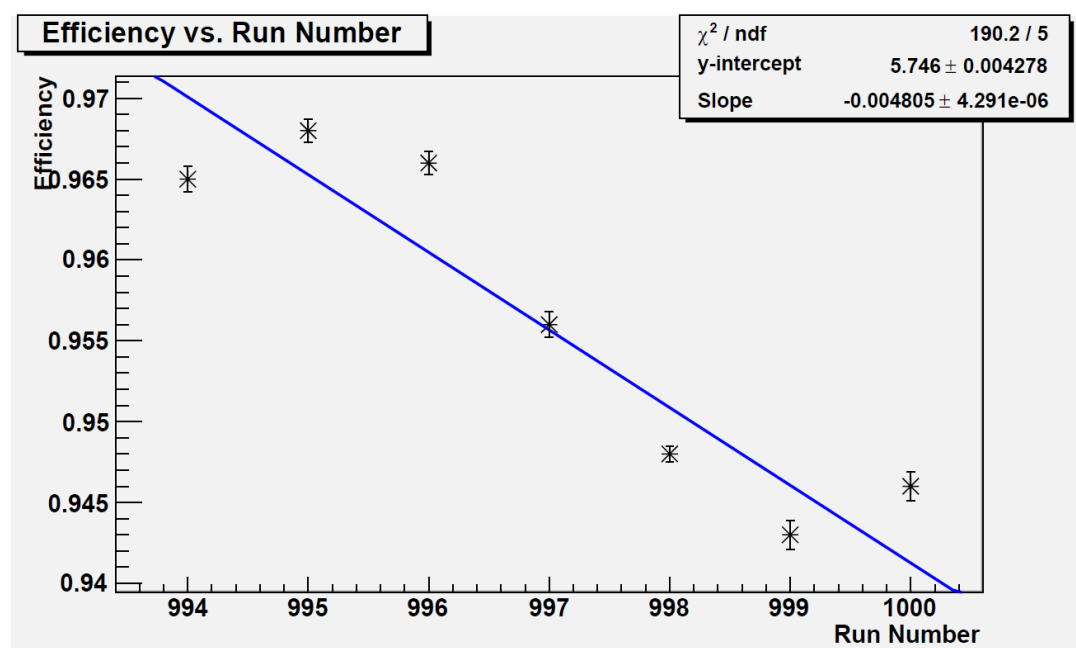


Figure 29: This plot is of the efficiency versus run number for a series of run immediately following pumping LC750 for 20 to 30 minutes. The only parameter allowed to change between these runs was the time the run was taken. The runs are around 2 to five minutes each. Since the precise time intervals are unknown, the exact value of the slope is not to relevant, although a rough time scale can be estimated at five percent per hour.

The efficiency jump mystery will likely persist, but useful results can still be drawn from this data. Each set of data is itself consistent with the expected behavior, and the offset is well defined (if not understood) by the data, so it is still reasonable to draw inferences from these data.

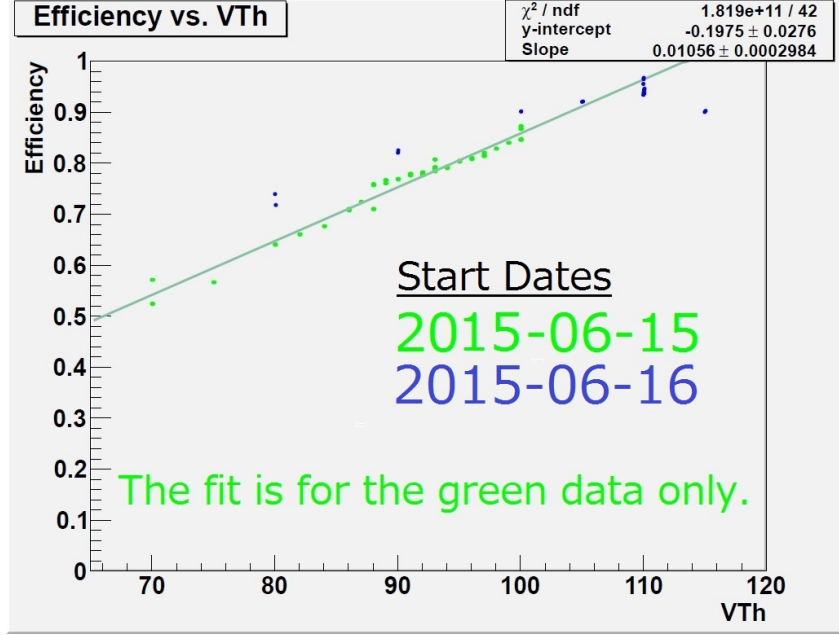


Figure 30: Above is the efficiency versus VTh data, plotted with a fit to the green points (from the first half of data collection). Extrapolating passed the noise floor, unit efficiency would be reached at VTh = 113.4, not far passed current noise floor.

As may be seen in (c) of Fig. 20, the efficiency at VTh = 115 is lower than the efficiency at VTh = 110. This is indicative of the threshold dropping too low, meaning near the noise floor. Multiple runs were done at these two threshold settings, and any deviation in efficiency due to unknowns in the run conditions is unlikely to account for this drop at VTh = 115. So there is high confidence that this is indeed the noise floor. If the efficiency were limited by something other than the noise floor, the efficiency would be expected to asymptote as a function of VTh, until eventually the noise floor was reached, at which point the efficiency would drop. As this is not seen, it is reasonable to believe that CMS ROCs with lower operational noise floors would allow diamond based particle sensors to perform with an efficiency closer to unity.

LC500 Analysis

Efficiency Analysis : VTh

After processing with Monicelli and Chewie, the data from LC500 were also examined. The efficiency versus VTh of LC500 was examined next, and in the same manner as was done for LC750. The initial efficiency versus VTh data was even more confusing than for LC750. The efficiency dropped to low values at some VTh values without a clear reason.

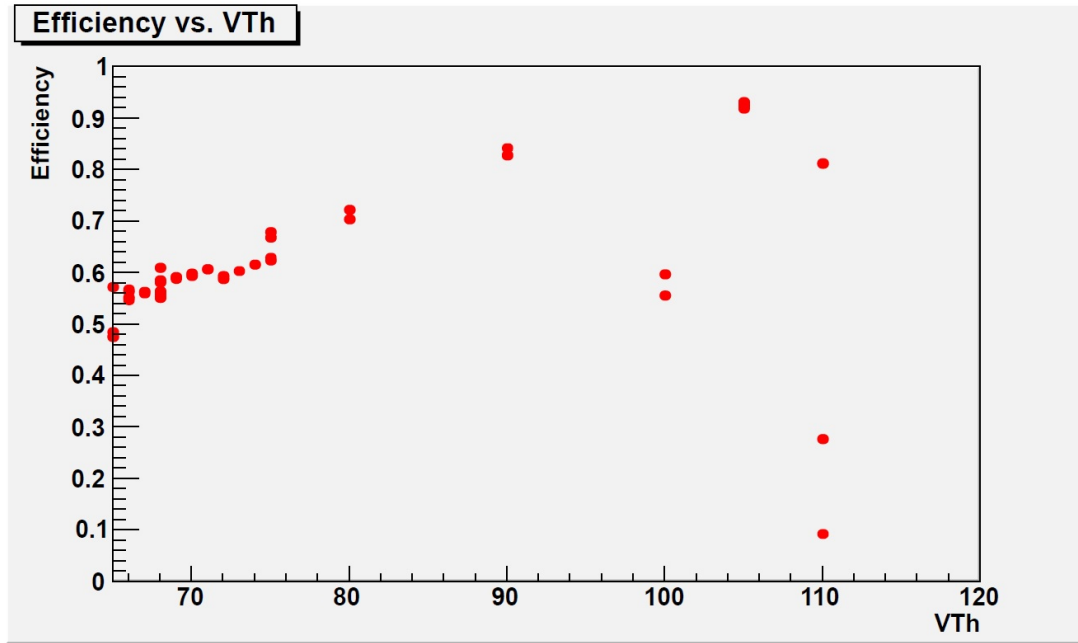


Figure 31: Above is a plot for LC500 and is of the efficiency versus VTh, at a high voltage of 500 V. As may be seen, the pattern become rather chaotic at VTh = 100 and above.

It was eventually discovered that the detector was giving out much more charge on some of the runs that are shown in the efficiency plot. The charge output for these runs was a factor of five or so greater than the normal levels, as determined by looking as the other runs. This deviation from the normal level suggests that these runs are contaminated by hot pixels and should be left out of the data to be analyzed.

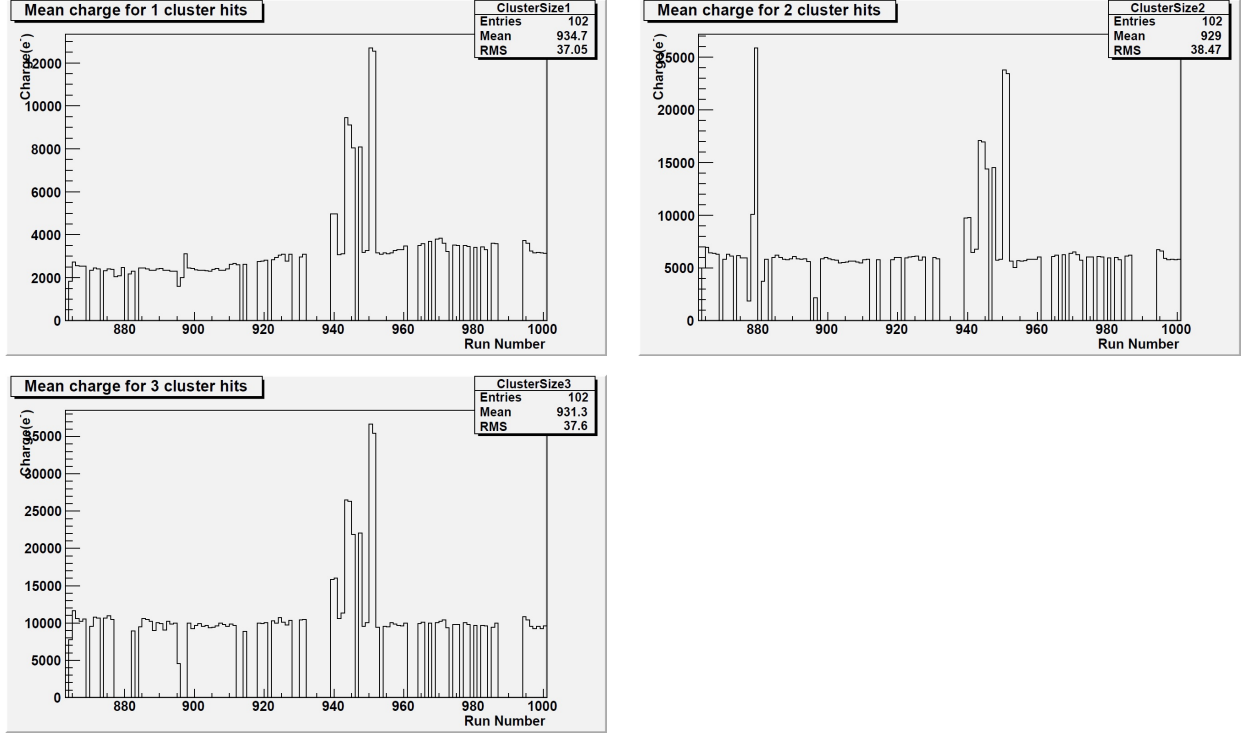


Figure 32: Above are plots of the mean charge for one hit clusters, two hit clusters, and three hit clusters. All three plots show a dramatic increase in the amount of mean charge around Run 950, and the two hit cluster plot shows an additional spike just before Run 880. These peaks are indicative of hot pixels. The cuts placed on the data from these plots were at $4000e^-$ for one hit clusters, $8000e^-$ for two hit clusters and $12000e^-$ for three hit clusters.

Removing these runs gets rid of the nonsensical data points, but also some of the data that looked correct, such as the points at $V_{Th} = 90$, or the highest efficiency point at $V_{Th} = 110$, which looked like it might indicate the noise floor. But these data points cannot be trusted and have thus been removed as well. These data do not show where the noise floor for LC500 is, so the LC500 data cannot corroborate LC750 in demonstrating that the efficiency is threshold limited. It does not contradict it either, and indeed makes it to 93.0 percent efficiency.

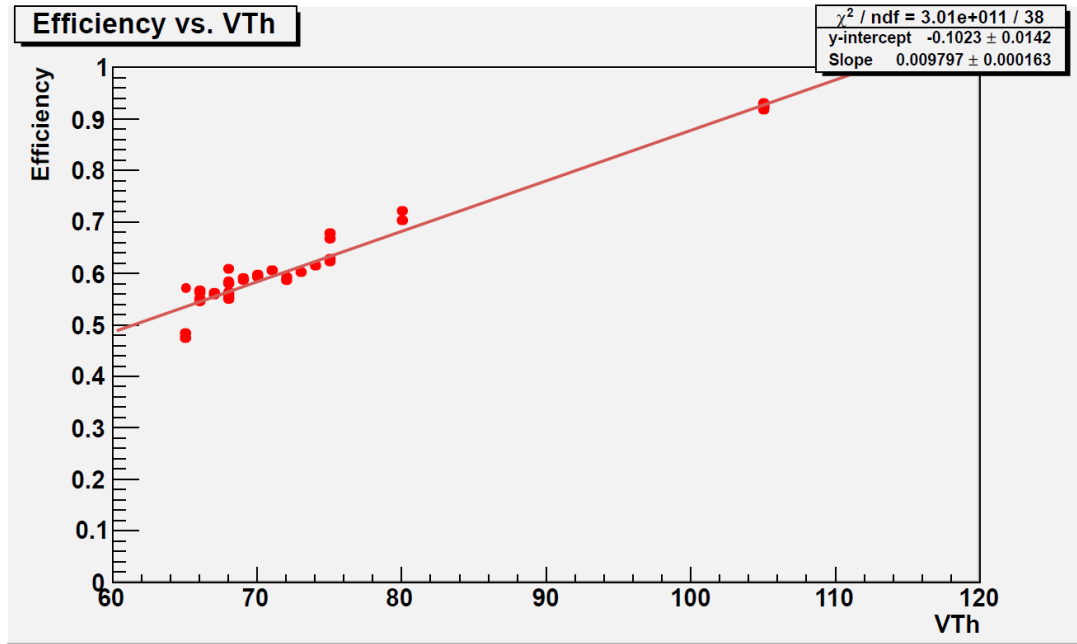


Figure 33: After applying a cut to remove the runs with hot pixels, the efficiency data looks reasonable. This is shown above. Additionally the data has been fit to a straight line. Following the line to where the efficiency is one, $V_{Th} = 112.5$.

There are other analyses that can be performed on LC500 despite not knowing where its noise floor was.

Efficiency Analysis : High; Voltage

High voltage scans were taken for LC500 as well, but unlike LC750, the data did not come out as cleanly. This is shown in Fig. 34. It is also important to note that these data have already underwent the removal of the noisy runs responsible for the problem in the efficiency analysis.

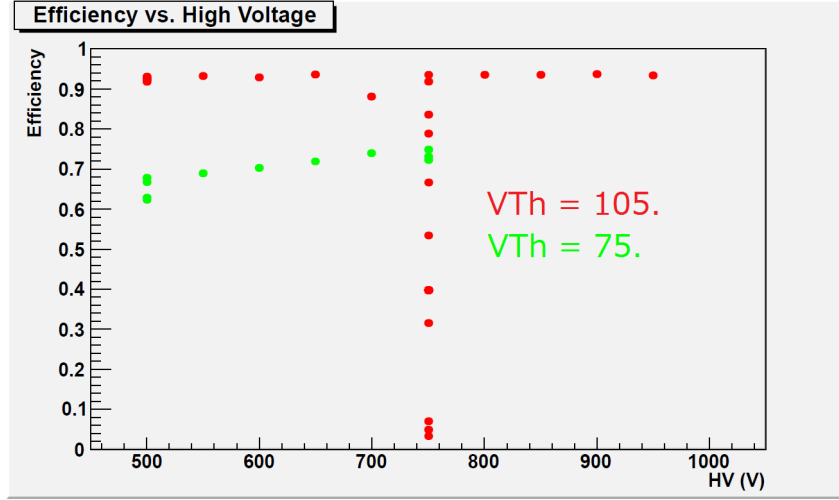


Figure 34: This is a plot of the efficiency versus high voltage LC500 data. The plot contains both the $V_{Th} = 75$ data (green), and the $V_{Th} = 105$ data (red). As may be evident, there is something peculiar at an applied voltage of 750 V, in that there are data from near zero to above 0.9.

As was the case for the ^{90}Sr lab bench tests, it was thought that this lack of convergence at a high voltage of 750 V, may be due to a CAPTAN problem. This was suspected during data acquisition. To test this hypothesis, the same data runs were analyzed for only the first half of the run. If the CAPTAN were misfiring non-uniformly, the full run and the half run would be expected to have different efficiencies.

Partial Run Efficiencies

Run Number	993	972
Full Run Efficiency	0.425 ± 0.002	0.918 ± 0.002
Half Run Efficiency	0.847 ± 0.003	0.921 ± 0.003

Figure 35: This table shows a sample of the LC500 full run/half run comparisons. These were chosen to illustrate the results found. Both runs are from the 750 V column in Fig. 34. The efficiency of Run 993 changes by nearly a factor of two, while that of Run 972 stays within statistical uncertainty. Run 993 has likely suffered from inconsistent CAPTAN performance and thus should be considered a invalid run.

Upon performing this analysis it became highly probable that this was indeed the case: runs with a efficiency roughly where it was expected to be were not significantly affected by using only half the run to determine the efficiency, while runs with atypically low efficiencies showed significant variations. A factor of two efficiency change was common.

This provided a criterion for identifying runs where the CAPTANs stopped shipping data: a ten percent difference between the full run efficiency and the half run efficiency was chosen as the criterion for a run to be considered invalid. After removing the invalid runs, the data were replotted and fit to straight lines. This is shown in Fig. 36.

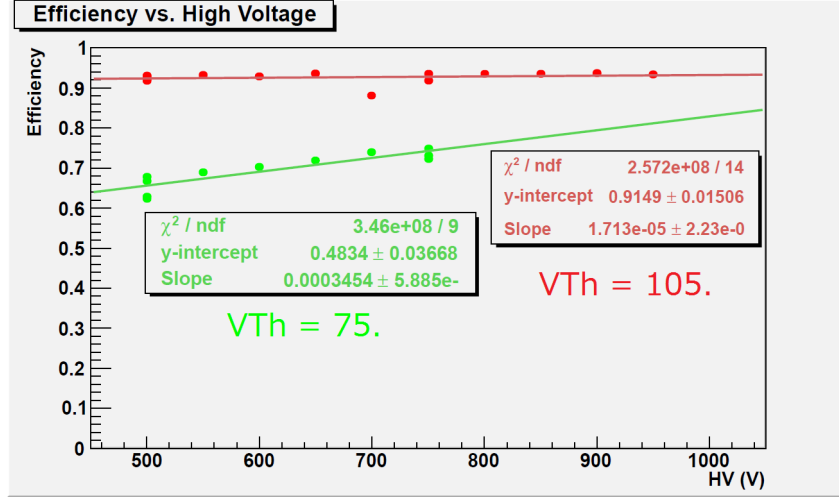


Figure 36: The LC500 efficiency versus high voltage data for $V_{Th} = 75$ (green), and $V_{Th} = 105$ (red) are shown. These data are fit to straight lines. Unlike the low threshold high voltage curves for LC750, and the lower threshold LC500 $V_{Th} = 105$ data, the higher threshold LC500 $V_{Th} = 75$ data shows a reasonable slope. So while increasing the voltage beyond the nominal $1V/\mu m$ has little effect at low thresholds it becomes helpful at high thresholds.

Efficiency Analysis : Gaps Between Pixels

LC500 was previously studied by [3], when it was on an older analog ROC. One of the analyses performed by [3], was to examine the efficiency between pixels. They found that when a particle traversed through the region between two pixels, any single pixel had a significant decrease in efficiency. This is because charges freed near the middle may be collected by the neighboring pixel. This means that the charge collected by either pixel may be below threshold. Still, by examining both the pointed to pixel, the pixel where the particle track is projected to intersect, and the adjacent pixel, the efficiency between the pixel could be increased. In [3], they studied both a single crystal diamond and the polycrystalline diamond LC500. They found that for the single crystal diamond the efficiency between pixels could be brought up to the efficiency in the center of the pixel

by this method. But for the polycrystalline LC500 the efficiency could not be increased as much.

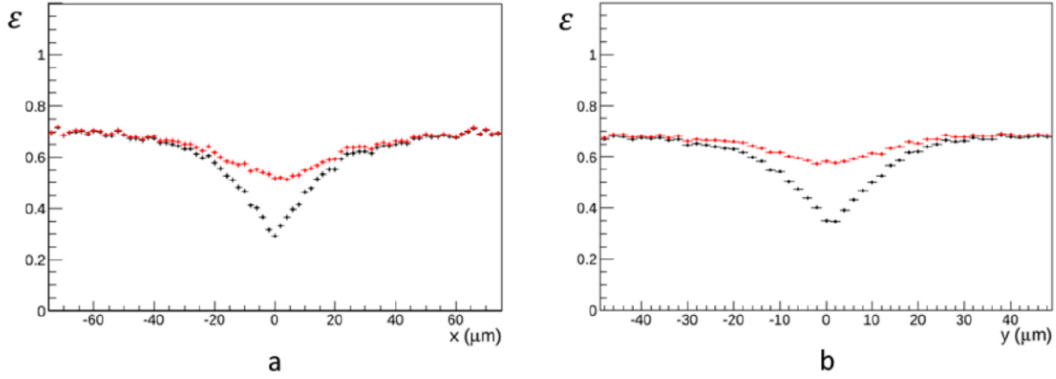


Figure 37: Above are two plots from a previous study of LC500 on the older analog ROC, conducted by [3]. In (a) the row efficiency is plotted; the black points are from efficiency measurements for a single pixel, while the red points have the charge from a neighboring pixel included. In (b) the same kind plot for the column data is shown. The dip in the middle is from the space in between pixels, where it is less likely that a single pixel will get enough charge to be above threshold.

This same data analysis was performed on the LC500 data from June 2015. Since LC500 was then on a new PSI digital ROC that is supposed to have a lower operating threshold, splitting the charge from an event between two pixels should have a lower probability of taking the charge a pixel sees below threshold. And so not only should the overall efficiency be higher, but the efficiency between pixels should decrease less. As can be seen in Fig. 38, the drop in efficiency between pixels is less when only one pixel is examined and can be almost eliminated when adjacent pixels are examined in tandem.

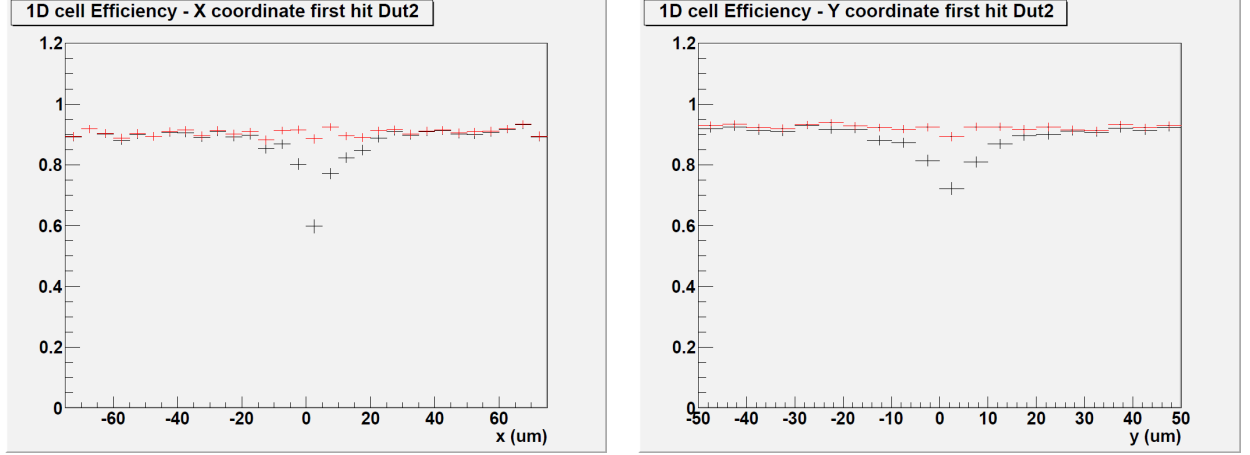


Figure 38: The above two plots again show the cell efficiencies for LC500 from one of the high efficiency Run 970. The row efficiency plot is on the left, and the column efficiency plot is on the right. The black points are for only a single pixel, while the red points add in the contribution from an adjacent pixel. Unlike the earlier study, the region in between pixels shows almost no efficiency drop when multiple pixels are considered. Since it is the exact same diamond, LC500, this difference can be attributed to the new digital ROC the diamond is mounted to. It should be noted that the dip does not reach its minimum at the zero in the spatial coordinate. This is because the detector's alignment was not perfect. While this puts an offset in where the pixels are located on the plots, the conclusions drawn should not be affected.

Conclusion

The switch to the new PSI digital ROCs increased the maximum obtainable efficiency. Both LC750 and LC500 reached efficiencies over 0.90, and displayed an efficiency that was predominately threshold limited. LC750 showed this behavior directly in the efficiency versus V_{Th} analyses. For LC750 the maximum efficiency it reached during the 2012 test beam was 0.844, while during the 2015 test beam the lower threshold ROC allowed it to reach an efficiency of 0.949. Although the noise floor of LC500 was possibly not reached, the reduced ROC threshold made preserving efficiency between pixels possible. In the study published by [3], the center of a pixel for LC500 was limited to an efficiency of about 0.64, while during the 2015 tests, the total efficiency of LC500 reached 0.926. The improvements for both DUTs almost certainly are due to the new digital ROCs with a lower operational threshold. For neither detector was it observed that the efficiency reached a saturation region where the efficiency versus V_{Th} asymptoted at high V_{Th} as would be expected if a saturation efficiency were reached. Based on these analyses it is reasonable to suggest that as CMS ROCs with a low enough noise floor become available, pCVD diamond as a vertex detecting medium may become a viable technology. Since LC750 is itself radiation damaged, diamond does appear to be a reasonably radiation hard detecting medium. To conclude, further investigation into diamond based sensor technology should investigate lower noise ROCs.

References

- [1] W. de Boer, et al., Phys. Status Solidi 204 (2007) 3004.
- [2] S. Schnetzer, et al, RD42 Collaboration, *Diamond Sensors for Energy Frontier Experiments*. (Proceedings of Science, Germany, 22nd International Workshop on Vertex Detectors, 15 Sept. 2013), pp. 1-10. http://pos.sissa.it/archive/conferences/198/029/Vertex2013_029.pdf
- [3] D. Menasce, et al, *Tracking performance of a single-crystal and a poly-crystalline diamond pixel-detector*. (IOP Science, Journal of Instrumentation, 10 June 2013), pp. 1-14. <http://iopscience.iop.org/article/10.1088/1748-0221/8/06/P06006/meta>
- [4] W. Adam, et al, RD42 Collaboration, *The first bump-bonded pixel detectors on CVD diamond*. (Science Direct, Nuclear Instruments and Methods in Physics Research A: Accelerators, Spectrometers, Detectors and Associated Equipment, Vol. 436, 1 Nov. 1999), pp. 326-335. <http://www.sciencedirect.com/science/article/pii/S0168900299005483>
- [5] L. L. Regal and W. R. Wilcox, *DIAMOND FILM DEPOSITION BY CHEMICAL VAPOR TRANSPORT*. (Science Direct, Acta Astronautica Vol. 48, 2 Jan. 2001), pp. 129-144. <http://www.sciencedirect.com/science/article/pii/S0094576500001557>
- [6] CVD Diamonds. www.cvd-diamond.com
- [7] J. E. Butler and I. Oletnik, *A mechanism for crystal twinning in the growth of diamond by chemical vapour deposition*. (The Royal Society, Philosophical Transactions of the Royal Society A, 28 Jan. 2008), pp. 1-17. <http://rsta.royalsocietypublishing.org/content/366/1863/295>
- [8] A. Mainwood, *CVD diamond particle detectors*. (Science Direct, Diamond and Related Materials, Vol. 7, Feb. 1998), pp. 504-509. <http://www.sciencedirect.com/science/article/pii/S0925963597002483?np=y>
- [9] T. Behnke, P. Huntemeyer, A. Oh, J. Steuerer, A. Wagner and W. Zenuer, *The charge collection properties of CVD diamond*. (Cornell University Library, High Energy Physics: Experiment, 15 April 1998), pp. 1-26. <http://arxiv.org/pdf/hep-ex/9804006v1.pdf>
- [10] K.A. Olive, et al, Particle Data Group, *Chinese Physics C*, fig. 32.1. (IOP Publishing, Bristol, UK, 2014), p. 399.
- [11] M. Guthoff, W. de Boer and S. Muller, *Simulation of beam induced lattice defects of diamond detectors using FLUKA*, (Cornell University Library, Physics: Instrumentation and Detectors, 25 Aug. 2013), pp. 1-8. <http://arxiv.org/pdf/1308.5419v1.pdf>
- [12] R. J. Tapper, *Diamond detectors in particle physics*. (IOP Science, Reports on Progress in Physics, Vol. 63, 2000), pp. 1273-1316. <http://iopscience.iop.org/article/10.1088/0034-4885/63/8/203/meta>
- [13] L. D. Landau, Ed. D. ter Haar, *Collected Papers of L. D. Landau: On the Energy Loss of Fast Particles by Ionization*. (Gordan and Breach, New York, 1965).

- [14] C.W. Fabjan, *DETECTORS FOR ELEMENTARY PARTICLE PHYSICS*. (CERN, Geneva, Switzerland, 25 Nov. 2014), p. 77-116. <https://cds.cern.ch/record/262454/files/p77.pdf>
- [15] M. Marucho, C.A. Canal and H. Fanchiotti, *THE LANDAU FOR CHARGED PARTICLES TRAVERSING THIN FILMS*. (Cornell University Library, High Energy Physics, 23 Oct. 2006), pp. 1-22. arXiv:hep-ph/0305310v3
- [16] ROOT: Data Analysis Framework, *Root Reference Guide*. (CERN, Geneva, Switzerland, 2015). https://root.cern.ch/doc/master/group_PdfFunc.html#ga53d01e04de833eda26560c40eb207cab
- [17] K.S. Kolbig and B. Schorr, *A PROGRAM PACKAGE FOR THE LANDAU DISTRIBUTION*. (Science Direct, Computer Physics Communications, Vol. 31, 1984) pp, 97-111. <http://www.sciencedirect.com/science/article/pii/0010465584900857>
- [18] M. Turqueti, R. Rivera, A. Prosser, J. Andresen and J. Chramowicz, *CAPTAN: A Hardware Architecture for Integrated Data Acquisition, Control, and Analysis for Detector Development*. (Fermi National Accelerator Laboratory, Electronic Systems Engineering Department, Batavia, Illinois), pp. 1-7. FERMILAB-PUB-08-527-CD
- [19] S. Terzo, *A Complete Package for Characterization of CMS-Upgrade Pixel Detectors at the Fermilab Test-Beam Facility*. Anno Accademico (2010-2011) pp 1-98.
- [20] Paul Scherrer Institut *PSI46 Pixel Chip - External Specification* (2004) pp 1-27